Persistent Sodium Current Drives Excitability of Immature Renshaw Cells in Early Embryonic Spinal Networks

Juliette Boeri, Hervé Le Corronc, François-Xavier Lejeune, Barbara Le Bras, Christine Mouffle, Monara Kaelle S.C. Angelim, Jean-Marie Mangin, Pascal Branchereau, Pascal Legendre, Antonny Czarnecki

HAL Id: hal-03220695

https://hal.sorbonne-universite.fr/hal-03220695v2

Submitted on 7 May 2021

JNeurosci
THE JOURNAL OF NEUROSCIENCE

Research Articles: Systems/Circuits

Persistent sodium current drives excitability of immature Renshaw cells in early embryonic spinal networks

Juliette Boeri[a], Hervé Le Corronc[a,b], François Xavier Lejeune[a], Barbara Le Bras[a], Christine Mouffle[a], Monara Kaelle S.C. Angelim[a], Jean Marie Mangin[a], Pascal Branchereau[c,d], Pascal Legendre[a] and Antonny Czarnecki a[a]

[a]INSERM, UMR_S 1130, CNRS, UMR 8246, Neuroscience Paris Seine, Institute of Biology Paris Seine, 75005 Paris, France. Sorbonne Univ, UPMC Univ Paris 06, UM CR18, 75005 Paris, France.

[b]Univ Angers, 49000 Angers, France.

[c]Bordeaux, INCIA, UMR 5287, F-33615 Pessac, France.

[d]CNRS, INCIA, UMR 5287, F-33615 Pessac, France.

1   **Persistent sodium current drives excitability of immature Renshaw cells in**
2   **early embryonic spinal networks**
3
4   **Abbreviated title:** I_{Nap} drives the excitability of newborn $V1^R$
5
6

7   **Juliette Boeri [a,1], Hervé Le Corronc [a,b,1] , François Xavier Lejeune [a], Barbara Le Bras [a],**
8   **Christine Mouffle [a], Monara Kaelle S.C. Angelim[a], Jean Marie Mangin[a], Pascal**
9   **Branchereau [c,d], Pascal Legendre [a,1], Antonny Czarnecki [a,1]**
10
11 [a] INSERM, UMR_S 1130, CNRS, UMR 8246, Neuroscience Paris Seine, Institute of Biology
12 Paris Seine, 75005 Paris, France. Sorbonne Univ, UPMC Univ Paris 06, UM CR18, 75005
13 Paris, France.
14 [b] Univ Angers, 49000 Angers, France.
15 [c] Univ. Bordeaux, INCIA, UMR 5287, F-33615 Pessac, France.
16 [d] CNRS, INCIA, UMR 5287, F-33615 Pessac, France.
17
18 Correspondence should be addressed to either of the following: Dr Antonny Czarnecki or Dr
19 Pascal Legendre, Institut National de la Santé et de la Recherche Médicale Unite Mixte de
20 Recherche S1130, Centre National de la Recherche Scientifique Unité Mixte de Recherche
21 8246, Université Pierre et Marie Curie, Bâtiment B, Etage 2, Boîte postale 37, 7 quai Saint
22 Bernard, 75005 Paris, France, E-mail: antonny.czarnecki@sorbonne-universite.fr or
23 pascal.legendre@inserm.fr.
24
25 **Number of pages:** 38
26
27 **Number of figures:** 10
28
29 **Number of tables:** 2
30
31 **Number of words:**
32 Abstract: 250
33 Introduction: 641
34 Discussion: 1492
35

42

ABSTRACT

Spontaneous network activity (SNA) emerges in the spinal cord (SC) before the formation of peripheral sensory inputs and central descending inputs. SNA is characterized by recurrent giant depolarizing potentials (GDPs). Because GDPs in motoneurons (MNs) are mainly evoked by prolonged release of GABA, they likely necessitate sustained firing of interneurons. To address this issue we analyzed, as a model, embryonic Renshaw cell ($V1^R$) activity at the onset of SNA (E12.5) in the embryonic mouse SC (both sexes). $V1^R$ are one of the interneurons known to contact MNs, which are generated early in the embryonic SC. Here, we show that $V1^R$ already produce GABA in E12.5 embryo, and that $V1^R$ make synaptic-like contacts with MNs and have putative extrasynaptic release sites, while paracrine release of GABA occurs at this developmental stage. In addition, we discovered that $V1^R$ are spontaneously active during SNA and can already generate several intrinsic activity patterns including repetitive-spiking and sodium-dependent plateau potential that rely on the presence of persistent sodium currents (I_{Nap}). This is the first demonstration that I_{Nap} is present in the embryonic SC and that this current can control intrinsic activation properties of newborn interneurons in the SC of mammalian embryos. Finally, we found that 5 µM riluzole, which is known to block I_{NaP}, altered SNA by reducing episode duration and increasing inter-episode interval. Because SNA is essential for neuronal maturation, axon pathfinding and synaptogenesis, the presence of I_{NaP} in embryonic SC neurons may play a role in the early development of mammalian locomotor networks.

64 **SIGNIFICANCE STATEMENT**

65 The developing spinal cord (SC) exhibits spontaneous network activity (SNA) involved in the

66 building of nascent locomotor circuits in the embryo. Many studies suggest that SNA depends

67 on the rhythmic release of GABA, yet intracellular recordings of GABAergic neurons have

68 never been performed at the onset of SNA in the SC. We first discovered that embryonic

69 Renshaw cells ($V1^R$) are GABAergic at E12.5 and spontaneously active during SNA. We

70 uncover a new role for persistent sodium currents (I_{NaP}) in driving plateau potential in $V1^R$

71 and in SNA patterning in the embryonic SC. Our study thus sheds light on a role for I_{NaP} in

72 the excitability of $V1^R$ and the developing SC.

73

74 **INTRODUCTION**

75   A remarkable feature of the developing central nervous system (CNS) is its capacity to

76 generate spontaneous network activity (SNA) at the end of neuronal migration. SNA occurs in

77 the absence of any external inputs and is not experience-driven or use-dependent (Moody,

78 1998; Feller, 1999). SNA has been described as playing an essential role in several areas of

79 the developing CNS, including the neocortex, the thalamus, the hippocampus, the locus

80 coeruleus, the retina and the spinal cord (Landmesser and O'Donovan, 1984; Ben-Ari et al.,

81 1989; Garaschuk et al., 1998; Feller, 1999; Garaschuk et al., 2000; Gust et al., 2003; Corlew

82 et al., 2004; Marder and Rehm, 2005; Myers et al., 2005; Gonzalez-Islas and Wenner, 2006;

83 Hanson et al., 2008; Rockhill et al., 2009; Watt et al., 2009). SNA regulates the development

84 of neural circuits by influencing synaptogenesis, neuronal maturation, axonal guidance and

85 axonal pathfinding (Zhang and Poo, 2001; Hanson et al., 2008; Kirkby et al., 2013).

86   In the embryonic spinal cord (SC), SNA is characterized by long-lasting bursts of action

87 potentials (APs) occurring every 2-4 min that can propagate along the cord (Hanson and

88 Landmesser, 2003). SNA occurs at the onset of synaptogenesis at E12.5, before the

89 emergence of functional neuromuscular junction and the formation of sensory and supra-

90 spinal inputs (Hanson and Landmesser, 2003). Bursts of APs recorded on ventral roots

91 (Hanson and Landmesser, 2003) or in the whole SC (Yvert et al., 2004) are long-lasting

92 episodes characterizing SNA in the embryonic SC. We previously showed that most

93 individual motoneurons (MNs) only generate a single AP during each episode of SNA

94 (Czarnecki et al., 2014) and we demonstrated that acetylcholine (ACh) release could not

95 directly synchronize MN firing during SNA as MNs do not express functional acetylcholine

96 receptors (Czarnecki et al., 2014). Therefore, MNs must rely on other mechanisms to

97 synchronize their firing during SNA. We have recently shown that MN activity occurring

98 during SNA at the onset of synaptogenesis (E12.5) is generated by giant depolarizing

99 potentials (GDPs) involving a massive and long-lasting release of GABA, as well as a

100   moderate release of glutamate and glycine (Czarnecki et al., 2014). It is therefore likely that

101   newborn GABAergic interneurons (INs) play an essential role in the generation of the

102   sustained episodes of depolarization necessary to synchronize MN firing during SNA.

103   To gain insight into the excitability pattern of spinal GABAergic INs involved in the

104   release of GABA during SNA, we used multiple approaches to examine the intrinsic

105   activation properties of immature Renshaw cells (V1^R) in the lumbar SC. Renshaw cells are

106   known to regulate MN activity in the adult through recurrent synaptic inhibition (Eccles et al.,

107   1956) and play an important role in the regulation of SC activity at late developmental stages

108   in the chicken embryo (Wenner and O'Donovan, 2001). V1^R are the first V1 INs to be

109   generated during neurogenesis in the mouse embryo (Benito-Gonzalez and Alvarez, 2012).

110   From E9.5 to E12.5, V1^R migrate toward their final location between MN columns and the

111   ventrolateral funiculus (Benito-Gonzalez and Alvarez, 2012; Alvarez et al., 2013). Because

112   glycine, unlike GABA, is nearly absent in SC INs of E12.5 mouse embryo (Allain et al.,

113   2004, 2006; Scain et al., 2010), V1^R are likely to be GABAergic neurons at the early

114   developmental stage.

115   Here, we show that, like MNs, V1^R display GDPs during SNA at E12.5. However, we

116   discovered that, unlike MNs, most V1^R are able to produce repetitive spiking or sodium-

117   dependent plateau potentials in response to GDPs (Czarnecki et al, 2014). Remarkably, these

118   sustained discharges depend on the presence of a persistent sodium current (I_{Nap}). In addition,

119   we also demonstrate that I_{Nap} already has important functions at the onset of SNA. Inhibition

120   of I_{Nap} alters SNA episode duration and inter-episode interval duration, which reveals that the

121   ability of embryonic SC neurons to generate sustained discharge is required for a correct SNA

122   pattern (Hanson and Landmesser, 2006).

123

124 **MATERIALS AND METHODS**

125 *Isolated spinal cord preparation*

126 These experiments were performed in accordance with European Community guiding

127 principles on the care and use of animals (86/609/CEE, CE Off J no. L358, 18 December

128 1986), French decree no. 97/748 of October 19, 1987 (J Off République Française, 20

129 October 1987, pp. 12245-12248) and recommendations from the CNRS. We used

130 GAD67eGFP knock-in mice to visualize putative GABAergic INs (Tamamaki et al., 2003).

131 Briefly, a cDNA encoding enhanced GFP (eGFP) was targeted to the locus encoding the gene

132 Gad1. GAD67 is a rate-limiting enzyme of GABA biosynthesis and is known to be a marker

133 for GABAergic neurons (Le Corronc et al. 2011). To obtain E12.5 GAD67-eGFP embryos, 8-

134 to 12-week-old wild-type Swiss female mice were crossed with heterozygous GAD67-eGFP

135 Swiss male mice. HB9-eGFP mouse embryos were used to visualize MNs (Wichterle et al.,

136 2002). To obtain E12.5 transgenic HB9-eGFP embryos, 8- to 12-week-old wild-type Swiss

137 female mice were crossed with heterozygous HB9-eGFP C57BL/6Jrj male mice.

138 269 embryos obtained from 152 pregnant mice were used. Isolated embryonic mouse

139 SCs were obtained as previously described (Delpy et al., 2008; Scain et al., 2010). Briefly,

140 pregnant mice were anesthetized by intramuscular injection of a mix of ketamine and xylazine

141 and sacrificed using a lethal dose of CO_2. Embryos of either sex were removed and the SC

142 was isolated from eGFP-positive embryos. Whole SCs were maintained in an artificial

143 cerebrospinal fluid (ACSF) containing 135 mM NaCl, 25 mM $NaHCO_3$, 1 mM NaH_2PO_4, 3

144 mM KCl, 11 mM glucose, 2 mM $CaCl_2$, and 1 mM $MgCl_2$ (307 mosmol/kg H_2O),

145 continuously bubbled with a 95% O_2-5% CO_2 gas mixture.

146

147 *Whole-cell recordings and analysis*

148 The isolated SC was placed in a recording chamber and continuously perfused (2

149 mL/min) at room temperature (20-24°C) with the oxygenated ACSF described above. Whole-

150   cell patch-clamp recordings of lumbar spinal $V1^R$ and MNs were carried out under direct

151   visualization using an infrared-sensitive CCD video camera.

152   In the SC of GAD67eGFP mouse embryos, eGFP neurons were detected using UV

153   light. MNs were identified by their size, their location in the ventral area of the SC

154   parenchyma (Czarnecki et al., 2014) and by the lack of eGFP expression. These neurons

155   localized in this SC area express the MN transcription factors Islet1/2, as shown in a previous

156   study (Scain et al, 2010). Recorded eGFP interneurons were localized in the ventrolateral area

157   of the SC at the marginal zone between motor columns and the ventral funiculus, which is the

158   known location of developing $V1^R$ (Stam et al., 2012). To confirm $V1^R$ identity, recorded

159   cells were filled with neurobiotin (0.5-1 mg/mL) and stained with an antibody directed against

160   Foxd3. Foxd3 is a specific transcription factor of V1 INs (Dottori et al., 2001; Stam et al.,

161   2012) and the hallmark of $V1^R$ localized in the ventrolateral area of the embryonic SC (Carr et

162   al., 1998; Benito-Gonzalez and Alvarez, 2012).

163   Whole-cell patch-clamp electrodes were pulled from thick-wall borosilicate glass using

164   a Brown-Flaming puller (Sutter Instrument Co., USA). The tip of the electrode was fire-

165   polished using a microforge (Narishige, Japan). Patch-clamp electrodes had resistances of 4-7

166   MΩ. The electrode was filled with a solution containing (in mM): 96.4 K methanesulfonate,

167   33.6 KCl, 4 $MgCl_2$, 4 Na_2ATP, 0.3 Na_3GTP, 10 EGTA, and 10 HEPES (pH 7.2; 290

168   mosmol/kg-H_2O). Using these potassium methanesulfonate solutions, the equilibrium

169   potential for chloride ions (ECl) ≈ -30 mV was close to the physiological values measured at

170   E12.5 on spinal MNs (Delpy et al., 2008). The junction potential (6.6 mV) was systematically

171   corrected offline. In some voltage-clamp experiments, the electrode contained: (in mM) 130

172   CsCl, 4 $MgCl_2$, 4 Na_2ATP, 10 EGTA and 10 HEPES (pH 7.2; 290 mosmol/kg-H_2O).

173   Signals were recorded using Axopatch 200B or Multiclamp 700B amplifiers (Molecular

174   Devices, USA). Data were low-pass filtered (2 kHz), digitized (20 kHz) online using a

175   Digidata 1440A interface and acquired using PClamp 10.5 software (pClamp,

176   RRID:SCR_011323). Analyses were performed off-line using PClamp 10.5 software and

177   Axograph X.1.6.4 (Axograph , RRID:SCR_014284).

178   In voltage-clamp or current-clamp experiments, neurons were recorded at a holding

179   potential (Vh) of -60 mV. Series resistance (10-20 MΩ) was monitored throughout the

180   experiments and was 50-80% compensated. Data were discarded if series resistance varied by

181   more than $\approx$ 30% from the initial value. In current-clamp mode, $V1^R$ intrinsic discharge

182   patterns were elicited using depolarizing current steps (from 0 to $\approx$ 50 pA, 2-10 pA

183   increments depending on the input resistance of the cell, 2 seconds) or depolarizing current

184   triangular-ramp (from 0 to $\approx$ 50 pA, 5 pA increments, 20 seconds) with an 8-second interval

185   to ensure that the membrane potential returned to baseline Vh. In voltage-clamp mode, whole-

186   cell currents were elicited by a depolarizing voltage ramp. The 70 mV/s speed was chosen to

187   elicit and measure persistent inward currents (I_{Nap}) (Huang and Trussell, 2008). Subtraction of

188   the current evoked by the voltage ramp in the presence of 1 μM TTX to control voltage ramp-

189   evoked current revealed I_{Nap}.

190   Action potentials or plateau potentials were analyzed based on the following parameters

191   during a 2-second current step: threshold potential, peak amplitude, half amplitude duration,

192   rate of rise of events (by dividing the amplitude of the event by the duration from its onset to

193   the peak; 2 seconds step width).

194   Boltzmann functions were used to describe I_{Nap} activation on current evoked by voltage

195   ramp. For the fit current (20 kHz sampling 2 KHz filter):

196

197    $G = G_{MAX}/(1+\exp(-(V-V_{HALF})/k))$

198

199   where G is conductance in nS, G_{Max} is the maximal conductance, V is the potential in mV,

200   V_{HALF} is the voltage for half-maximal activation in mV, and k is the slope factor in mV.

201   Threshold for activation I_{Nap} was determined by eye from Boltzmann curves.

202

Extracellular recordings

204   In the same experimental conditions as for whole-cell recordings, spontaneous activity

205   was recorded extracellularly from E12.5 SCs using glass electrodes. Extracellular electrodes

206   were placed under visual control on the superficial part of the ventral horn both at the cervical

207   and the lumbar levels. Targeted networks likely include MNs as well as surrounding INs

208   (Czarnecki et al., 2014). Electrodes were connected to a high-gain a.c. amplifier (ISO-

209   DAM8A-4 Bio-amplifier System, World Precision Instruments Ltd, Stevenage, UK). Filtered

210   (Filter cutoff frequency: 0.3-3 kHz) raw signals were integrated off-line and analyzed using

211   Spike2 software (Spike2 Software, RRID:SCR_000903). Changes in burst duration and

212   maximum instantaneous frequency were calculated from cervical and lumbar recordings.

213

Pharmacological agents

215   During patch-clamp recordings, drugs were applied using 0.5 mm diameter quartz

216   tubing positioned 50 μm away from the recording area under direct visual control. The quartz

217   tubing was connected using a manifold to 6 solenoid valves linked with 6 reservoirs.

218   Solutions were gravity-fed into the quartz tubing. Drug application was controlled using a

219   VC-8 valve controller (Warner Instruments, USA). The following pharmacological agents

220   were used: tetrodotoxin (TTX) (1 μM, Alomone, Israel) and riluzole (5-10 μM Tocris

221   Bioscience, UK). Both were dissolved in the bath solution.

222

Immunohistochemistry

224   All primary antibodies used and their respective dilutions are listed in Table 1. E12.5

225   embryos were collected from pregnant females. Once dissected out of their yolk sac, these

226   embryos were immediately immersion-fixed in phosphate buffer (PB 0.12 M) with 4%

227   paraformaldehyde (PFA; freshly prepared in PB, pH 7.4) for 1 h at 4°C. Embryos were then

228   rinsed with PB and cryoprotected in PB-15% sucrose at 4°C for 24 h and then in PB-30%

229   sucrose at 4°C for 24 h. Embryos were embedded in OCT medium (VWR, Fontenay-sous-

230   Bois, France) and quickly frozen. Serial sections 20 μm thick were collected onto slides using

231   a cryostat. Immunostaining was processed on SC transverse sections and on whole SC post-

232   recording to confirm IN identity. To reveal neurobiotin-labeled cells, SCs were fixed for 1 h

233   in 4% PFA and were then incubated in 0.12 M PB at 4°C until immunohistochemical studies.

234   Tissues (embryo slices and whole SC) were thawed at room temperature, washed in PBS,

235   incubated in NH_4Cl (50 mM) diluted in PBS for 20 min and then permeabilized for 30 min in

236   a blocking solution (10% goat serum in PBS) with 0.2% Triton X-100 and then for 48 h at

237   4°C with the primary antibodies, which were diluted in the 0.2% Triton X-100 blocking

238   solution. Slices or whole SCs were then washed in PBS and incubated for 2 h at RT in the

239   secondary antibodies (diluted at 1/1000 in the 0.2% Triton X-100 blocking solution): Alexa

240   Fluor 405 (Thermo Fisher Scientific Cat# A-31556, RRID:AB_221605) or 647 goat anti-

241   rabbit (Thermo Fisher Scientific Cat# A-21244, RRID:AB_2535812); Alexa Fluor 594 goat

242   anti-guinea pig (Thermo Fisher Scientific Cat# A-11076, RRID:AB_2534120); Alexa Fluor

243   649 donkey anti-guinea pig (Jackson ImmunoResearch Labs Cat# 706-605-148,

244   RRID:AB_2340476); Alexa Fluor 594 goat anti-mouse (Thermo Fisher Scientific Cat# A-

245   11005, RRID:AB_2534073); Alexa Fluor 488 goat anti-chicken (Thermo Fisher Scientific

246   Cat# A-11039, RRID:AB_2534096) and streptavidin-conjugated Alexa Fluor 405 (1:1000,

247   Thermo Fisher Scientific Cat# S32351). After washing in PBS, slides or whole SCs were

248   dried and mounted in Mowiol medium (Millipore, Molsheim, France).

249

250   ***Confocal microscopy and image analysis***

251   Preparations were analyzed using a Leica SP5 confocal microscope. Immunostaining

252   was observed using a 40X oil-immersion objective with a numerical aperture of 1.25, as well

253   as with a 63X oil-immersion objective with a numerical aperture of 1.32 and a 4X digital

254   zoom magnification. Serial optical sections were obtained with a Z-step of 1 μm (40X) and

255   0.2-0.3 μm (63X). Images (1024x1024; 12-bit color scale) were stored using Leica software

256   LAS-AF and analyzed using ImageJ 1.5 softwares (<u>Wright Cell Imaging Facility</u>,

257   RRID:SCR_008488). Colocalization of synaptophysin staining with calbindin staining, eGFP

258   staining (MNs; HB9eGFP mouse embryos) or neurobiotin staining was assessed in 3 axes

259   using a single confocal slice and X and Y orthogonal views of the stack (ImageJ 1.5).

260

261   ***Sniffer recordings.***

262   To make a "sniffer" electrode (Young and Poo, 1983) for GABA, an outside-out patch

263   was pulled from a transfected HEK293 cell line expressing the $GABA_AR$ subunits α3β2γ2

264   (kindly provided by Michel Partiseti, Sanofi Advantis R&D LGCR/LIT, France). This

265     $GABA_AR$ is highly specific for GABA and is characterized by slow desensitization, which

266   makes it a good sensor for GABA paracrine release (Barberis et al., 2007). As a control, the

267   electrode was first positioned outside the SC to verify any GABA contamination in the

268   recording medium. The electrode was then pushed inside the SC and positioned within the

269   motoneuronal area and the ventral funiculi. Outside-out patch-clamp electrodes (5-10 MΩ)

270   were pulled from thick-wall borosilicate glass, fire-polished and filled with (in mM): CsCl

271   130, $MgCl_2$ 4, Na_2ATP 4, EGTA 10, HEPES 10 (pH 7.2, osmolarity 290 mosmol/kg-H_2O).

272   Single channel currents were recorded using an Axopatch 200B amplifier (Molecular

273   Devices, USA). Recordings were filtered at 10 kHz, sampled at 50 kHz and stored on a PC

274   computer. Membrane potential was held at -50 mV throughout the experiment. Analysis of

275   the sniffer currents was performed using Axograph X.1.6.4 software.

276   Human embryonic kidney 293 cells (HEK293) were maintained in a 95% air - 5% CO_2

277   humidified incubator, at 35°C, in Dulbecco's modified Eagle's medium supplemented with

278   0.11 g/L sodium pyruvate, 6 g/L D-glucose, 10% (v/v) heat-inactivated fetal bovine serum (all

279   from Gibco BRL). Cells were passaged every 5-6 days (up to maximum 20 times). For

280   electrophysiological recordings, cells were seeded onto glass coverslips coated with poly-L-

281   ornithine (0.1 mg/mL).

282   ***Statistics***

283   All values were expressed as mean ± standard deviation. Statistical significance was

284   assessed by the non-parametric Kruskal-Wallis test with Dunn's post tests, Mann-Whitney

285   test and Wilcoxon matched pairs test (GraphPad Prism 5.0 Software, USA). Significance was

286   determined as $P < 0.05$ (*), $P < 0.01$ (**) or $P < 0.001$ (***).

287 **RESULTS**

288 *V1^R are identified with calbindin, Foxd3 and MafB at the onset of SNA.*

289   In the present study, we used GAD67-enhanced green fluorescent protein (eGFP)

290 knock-in mice (Tamamaki et al., 2003) to visualize putative GABAergic INs (Figures 1A1,

291 1B1 and 1C1). V1^R can be unambiguously identified by their characteristic position in the

292 ventral horn both in the adult (Geiman et al., 2000) and in the embryo (Sapir et al., 2004;

293 Stam et al., 2012). Most V1^R were localized between the ventral border of MN columns and

294 the ventral funiculi. To identify V1^R in the lumbar SC of E12.5 GAD67eGFP embryos, we

295 first performed immunostaining using anti-calbindin, anti-Foxd3 and anti-MafB antibodies

296 (Figure 1). Calbindin is a calcium-binding protein exclusively expressed by V1^R when

297 looking in the ventrolateral area of the SC between the MN columns and the funiculus (Stam

298 et al., 2012). The forkhead transcription factor Foxd3 controls the early phase of V1^R

299 differentiation, whereas MafB is required to maintain V1^R at later developmental stages, and

300 both are therefore expressed at E12.5 in V1^R (Stam et al., 2012). At E12.5 INs located in the

301 ventrolateral marginal zone between the motor columns and the ventral funiculi express

302 Foxd3 (Figures 1A2, 1B2 and 1C2) and calbindin (Figures 1A3 and 1B3), as previously

303 described (Stam et al., 2012; Benito-Gonzalez et al, 2012). Foxd3$^+$ INs were also observed in

304 neurons positioned dorsally to the motor columns (Figures 1A2 and 1B2). However, these INs

305 were not stained by calbindin antibody, hence this population of INs was not included in our

306 study. In the V1^R area, double immunostaining (Figures 1A4 and 1B4) indicated that 81.7 $\pm$

307 15.0% of Foxd3$^+$ INs localized in the ventral marginal zone were also immunoreactive to

308 calbindin at E12.5 (n=4 embryos, 2 sections/embryo). To ensure that all Foxd3$^+$ INs localized

309 in the area are V1^R, we performed double immunostaining using anti-Foxd3 and anti-MafB

310 antibodies (Figures 1C). We found that 100% of Foxd3$^+$ eGFP$^+$ INs localized in the ventral

311 marginal zone were also immunoreactive to anti-MafB antibody (n = 4 embryos, 2

312 sections/embryo), thus confirming their V1^R fate (Figure 1C4). It should also be noted that at

313   this developmental stage we detected MafB[+] eGFP^{-} neurons localized within the motor

314   columns (Figures 1C1 and 1C3) that are likely MNs (Stam et al., 2012). Therefore, we used

315   Foxd3 immunostaining to confirm that the recorded IN belonged to the V1^R population

316   (Figures 1D1, 1D2, 1D3 and 1D4). Whereas Calbindin is a good marker for V1^R, it was not

317   used to identify recorded V1^R because of cytoplasm-calbindin dilution complications during

318   whole-cell recording (Muller et al., 2005), caused by the high nucleus/cytoplasm volume ratio

319   in embryonic neurons.

320

321   *V1^R already produce GABA at E12.5.*

322   As calbindin is localized within the cytoplasm of V1^R, we used calbindin

323   immunostaining to visualize V1^R morphology (Stam et al., 2012). $96.6 \pm 7.2\%$ of calbindin[+]

324   neurons in the ventrolateral marginal zone were also eGFP[+] in E12.5 GAD67eGFP knock-in

325   mouse embryos (n = 4 embryos, 2 sections/embryo), which could suggest that most V1^R are

326   likely to produce GABA at this developmental stage. To determine to what extent V1^R already

327   produce GABA at E12.5, we performed double immunostaining using anti-calbindin and anti-

328   GABA antibodies (Figures 2A and 2B). We found that $90.1 \pm 10.5\%$ (n = 8 embryos, 2

329   sections/embryo) of calbindin[+] INs localized in the ventrolateral marginal zone (Figures 2A2

330   and 2B2) were also immunoreactive to GABA antibody (Figures 2A3, 2A4, 2B3 and 2B4),

331   suggesting that V1^R already produced enough GABA to be detected by

332   immunohistochemistry at E12.5.

333   It is important to note that many eGFP[+] GABA[-] INs were detected within the ventral

334   parenchyma at E12.5, as previously observed (Allain et al., 2004). This could result from the

335   production of the GAD67 splice variant GAD25. At early developmental stages, GAD1 first

336   encodes the truncated 25-kDa leader (GAD25) without GAD enzymatic activity and then the

337   enzymatically active protein GAD44 (see for review (Le-Corronc et al., 2011). These two

338   GAD isoforms are down-regulated during neuronal differentiation concomitantly with up-

339   regulation of GAD67 expression.

340

341   ***Synaptic-like contacts are detected between V1^R and MNs at the onset of SNA***

342   At E12.5, V1^R axons are localized in ventral funiculi and extend for a few segments

343   without forming collateral branches entering the motor columns (Alvarez et al., 2013). The

344   first evidence for collateral V1^R axons innervating the soma of lumbar MNs was found at

345   E15.5 only while synaptic-like connections from MNs onto the V1^R cell body were already

346   observed at E12.5 (Alvarez et al., 2013). Accordingly, it was proposed that MNs can control

347   V1^R activity at E12.5 while V1^R are unable to control MN activity at this time point (Alvarez

348   et al., 2013). However, it should be noted that synaptophysin staining was found mainly in the

349   ventral funiculus at E12.5 (Figure 3A1) (Alvarez et al., 2013; Czarnecki et al., 2014), where

350   IN axonal projections and MN dendrite-like processes were observed (Czarnecki et al., 2014).

351   Accordingly, we hypothesized that V1^R already make some synaptic-like contacts with MN

352   projections within the ventral funiculus.

353   To address this issue we first performed multiple immunostaining using anti-synaptophysin

354   antibody (putative release site), anti-calbindin antibody (V1^R) and anti-eGFP antibody on

355   coronal sections of the SC HB9eGFP mouse embryos to visualize MNs (Figures 3A2, 3A3,

356   3A4, 3B1, 3B2 and 3B3). As shown in Figure 3B3, many calbindin$^+$ fibers were apposed to

357   MN neurites (eGFP staining) within the ventral funiculus. We found 21.7 ± 8.4

358   synaptophysin$^+$ punctates within calbindin$^+$ fibers apposed to MN neurites per hemi section in

359   coronal slices (n = 9; 5 embryos) (Figures 3B1, 3B2 and 3B3; inserts, arrow). Conversely,

360   synaptophysin punctates were also found in MN fibers (eGFP$^+$) apposed to calbindin$^+$ fibers

361   (Figures 3B1, 3B2 and 3B3; insert, arrow head), which indicate the presence of MN putative

362   release sites apposed to V1^R within the ventral funiculus. We also found synaptophysin

363   punctates within calbindin$^+$ fibers that were not apposed to MN neurites (Figures 3B1, 3B2

364   and 3B3; barred arrow). This may indicate the presence of non-synaptic release sites and/or

365 that V1^R can make contact with fibers of neurons other than MNs. To further confirm the

366 presence of V1^R synaptic-like contacts on MNs, we performed multiple immunostaining using

367 anti-synaptophysin antibody (putative release site) and anti-eGFP antibody on isolated SC

368 after patch-clamp injection of neurobiotin in V1^R (Figures 3C). Recorded INs (eGFP negative)

369 in eGFP HB9 embryos were identified as V1^R using Foxd3 immunostaining (Figure 3C1;

370 insert). We found 3 to 5 putative release sites per V1^R (n = 4 cells) that were apposed to MN

371 fibers within the ventral funiculus (Figures 3C1, 3C2, 3C3 and 3C4). We did not find any

372 release site within the V1^R axonal growth cone (data not shown).

373

374 ***Paracrine release of GABA occurred in the SC of E12.5 mouse embryos.***

375   Paracrine release of GABA may occur from non-synaptic release sites and/or may

376 reflect neurotransmitter spillover of GABA from immature synapses (Safiulina and

377 Cherubini, 2009). Therefore, we hypothesized that GABA release can occur at this

378 developmental stage. To detect the presence of GABA paracrine release, we used the sniffer

379 technique (Scain et al., 2010). Outside-out patches from HEK cells expressing the GABA$_A$R

380 subunits α3β2γ2 were used as a "sniffer" to detect the presence of GABA in the extracellular

381 space (Figure 4 A1). When inserting the sniffer electrode in the vicinity of MNs, we did not

382 detect any GABA$_A$R, thus indicating that basal GABA concentration is below the detection

383 threshold of the sniffer patch (data not shown). The possibility of evoking GABA release, and

384 hence GABA$_A$R activation, by inducing a global cell membrane depolarization was tested

385 using bath application of 30 mM KCl (Scain et al., 2010; Czarnecki et al., 2014). Increasing

386 $[K^+]_o$ evoked a significant GABA$_A$R activation in the sniffer patch (n = 9), indicating that

387 GABA can be released in the extracellular space in response to cell membrane depolarization

388 (Figure 4 A1). We estimated the concentration of released GABA around MNs by comparing

389 the peak amplitude of the sniffer response evoked by KCl application to sniffer responses

390 evoked by exogenous application of 3, 10 and 30 μM GABA onto the same outside-out patch

391 (n = 9). We found that the GABA concentration accounting for $GABA_AR$ activity evoked by

392 KCl application was close to 3 μM (Figure 4 A2). Although the estimated concentration of

393 non-synaptic release of GABA was relatively low, the exogenous application of 3 μM GABA

394 in the presence of 1 μM TTX was sufficient to evoke a 20.6 ± 6.1 mV MN depolarization (Vh

395 = -60 mV; ECl = -30 mV; n = 7) (Figures 4B2).

396

397 *$V1^R$ exhibit heterogeneous excitability patterns at the onset of SNA.*

398 Spontaneous or evoked RC activity was assessed using whole-cell current-clamp

399 recordings and the open-book SC preparation (Scain et al., 2010). To determine the identity of

400 recorded INs, GAD67eGFP neurons were filled with neurobiotin (≈ 1 mg/mL) in combination

401 with post-hoc Foxd3 staining (Figures 1D). At E12.5, $V1^R$ had a whole-cell capacitance of

402 13.7 ± 3.8 pF (n = 192) and an input resistance of 1242 ± 620 MΩ (n = 192). Spontaneous

403 activity recorded in 37 $V1^R$ was characterized by recurrent GDPs (Figure 5), occurring every

404 3.7 ± 2.4 min (n = 30), similar to what has been observed in MNs (~3 min) (Czarnecki et al.,

405 2014). Interestingly, in 21.6% (n = 8/37) of the recorded $V1^R$, GDPs evoked long-lasting

406 depolarizing plateau potentials (Figure 5A), while 37.8% (n = 14/37) of the recorded $V1^R$ had

407 the ability to spike repetitively during GDPs (Figure 5B). Plateau potentials had an absolute

408 amplitude of 53.4 ± 11.5 mV (n = 8) and a half amplitude duration ranging from 0.12 to 0.86

409 s (0.44 ± 0.22 s; n = 8). In 16.2% (n = 6/37) of the recorded $V1^R$, GDPs evoked a single spike

410 or a doublet (figure 5C), while the remaining 24.3% (n = 9/37) of the recorded $V1^R$ did not

411 spike during GDPs (data not shown). These data show that $V1^R$ can generate various

412 spontaneous activity patterns and raise the question of their intrinsic activation properties.

413 To analyze the intrinsic activation properties of embryonic $V1^R$, we depolarized the

414 cells from a holding potential of -60 mV using 2 s step current pulses or 20 s depolarizing

415 current ramps. At E12.5, all $V1^R$ were excitable (n = 164), but depolarizing current injections

416 triggered various and complex excitability patterns (Figure 6). 28.7% (n = 47/164) of the

417   analyzed $V1^R$ were able to generate 1 to 3 action potentials (APs) in response to

418   suprathreshold depolarizing steps (Figure 6A). When a depolarizing ramp was applied, only

419   fast membrane potential oscillations of small amplitude were observed. We called these $V1^R$,

420   SS-$V1^R$, ("single" spiking $V1^R$,). In contrast, 21.2% (n = 36/164) of the recorded $V1^R$ were

421   able to generate long-lasting events defined as plateau potentials in response to depolarizing

422   current pulses and in response to depolarizing current ramps. These plateau potentials were

423   all-or-none events (Figure 6B). They can be evoked by long depolarizing pulses (2s) (Figure

424   6B) and short depolarizing current pulses (Figure 6F2). They had a half amplitude duration of

425     $\approx$ 700 ms and an absolute peak amplitude of $\approx$ 3 mV (Table 2). Remarkably, these plateau

426   potentials were sodium-dependent events as they were fully blocked by the application of 1

427   μM TTX (Figure 6F1). Unlike SS-$V1^R$, these $V1^R$ can generate repetitive plateau potentials

428   when depolarized by a suprathreshold depolarizing current ramp (Figure 6B). We called these

429     $V1^R$, PP-$V1^R$ (plateau potential $V1^R$). A third group of $V1^R$ (41.5%; n = 68/164) was

430   identified based on their ability to generate repetitive AP firing in response to suprathreshold

431   depolarizing current steps or to depolarizing current ramps. In these cells, APs had a half

432   amplitude duration $\approx$ 13 ms (Table 2). We called these $V1^R$, RS-$V1^R$ (repetitive spiking $V1^R$)

433   (Figure 6C). Finally, a fourth group of cells (8.5%; n = 14/164) was determined according to

434   their ability to generate both APs and plateau potential-like events (Figure 6D). We called

435   these $V1^R$, ME-$V1^R$ (mixed event $V1^R$). SS-$V1^R$ are unlikely to be dying neurons.

436   Developmental cell death (DCD) of V1 INs occurs after E14.5 in mouse embryos (Prasad et

437   al., 2008) and SS-$V1^R$ passive electrical properties did not differ from those of more active

438     $V1^R$ (Table 2).

439   Considering that the different types of intrinsic activation pattern may reflect a

440   continuum between a single spike and a plateau potential, we chose to focus our study on the

441   three clear patterns of intrinsic activation, SS-$V1^R$, RS-$V1^R$ and PP-$V1^R$, and to not study the

442   mixed regime in depth. Table 2 summarizes passive and active intrinsic electrical properties

443 of recorded SS-V1^R, RS-V1^R and PP-V1^R. Note that the difference in intrinsic excitability in

444 these different classes of V1^R is not due to difference in their membrane resistance ($P > 0.1$).

445 These results reveal that V1^R can have different regimes of activity in the embryonic SC

446 at the onset of synaptogenesis and SNA (E12.5) (Scain et al., 2010; Czarnecki et al., 2014).

447

448 *Sustained discharge in embryonic V1^R depends on persistent sodium current.*

449 A key element in neurons, which exhibit sustained discharges, is the expression of

450 subthreshold slow-inactivating inward currents. Among these inward currents, the TTX-

451 sensitive persistent inward current (I_{Nap}) plays a fundamental role in controlling sustained

452 discharge in INs and MNs in the SC at postnatal developmental stages (Lee and Heckman,

453 1998; Kuo et al., 2006; Theiss et al., 2007; Ziskind-Conhaim et al., 2008).

454 To determine whether I_{Nap} is already expressed by V1^R in E12.5 mouse embryo, we

455 made whole-cell voltage-clamp recordings. In this set of experiments, the electrodes were

456 filled with a Cs-based intracellular solution to minimize contamination of the recorded current

457 by potassium currents. A test pulse from -100 to -20 mV evoked TTX-sensitive sodium

458 currents: a large amplitude transient current (I_{NaT}) followed by a smaller amplitude current

459 persisting over 0.5 s was also fully blocked by TTX (Figure 7A1, inset), which indicates the

460 presence of I_{Nap}. This also indicates that sodium-independent voltage-gated inward currents

461 were not detected at this developmental stage. To characterize I_{Nap} better, we used a slow

462 voltage ramp (70 mV/s) from -100 to +20 mV designed to inactivate transient currents

463 (Huang and Trussell, 2008). Subtraction of the trace after TTX application revealed the I_{Nap}

464 on the I-V curve (Figure 7A1). I_{Nap} was observed in all recorded RCs. We further investigated

465 the activation properties of the I_{Nap}. The Boltzmann fit of the voltage dependence of the I_{Nap}

466 generated by voltage ramps revealed a V_{half} of -22.9 ± 5.7 mV and a slope factor (k) of 7.0 ±

467 1.8 mV in RCs (n = 8) (Figure 7A2). In RCs, the I_{Nap} activated at Vh = -67.4 ± 6.2 mV (n = 8)

468 and the mean persistent sodium conductance density (g_{NaP}/pF) was 41.8 ± 22.7 pS/pF (n = 12)

469 (Figure 7B).

470 To further confirm that this persistent inward current truly reflects the presence of I_{Nap},

471 we tested the effect of a low concentration of riluzole (5 µM), which is known to block I_{Nap}

472 (Urbani and Belluzzi, 2000). Indeed, 5 µM riluzole suppressed $81.5 \pm 14.6\%$ (n = 15; $P =$

473 0.0005) of the I_{Nap} in $V1^R$ (Figure 7C), whereas at this low concentration riluzole only slightly

474 reduced the peak amplitude of I_{NaT} (see red arrows in Figure 7A1, inset). We confirmed on

475 MNs that this low concentration had a minimal effect on the sodium-dependent AP, which

476 was not the case when riluzole concentration was increased to 10 µM (Figures 8A and 8B1-

477 B3). AP amplitude was significantly reduced to $83.2 \pm 12.6\%$ of control in the presence of 5

478 µM riluzole (n = 7; $P = 0.008$), but was reduced to $67.5 \pm 17.0\%$ of control when riluzole

479 concentration was increased to 10 µM (n = 7, $P = 0.0078$). We then reasoned that the lack of

480 repetitive spiking or plateau potential activity observed in some $V1^R$ might depend on a

481 reduced level of I_{Nap}. To test this hypothesis, we compared the presence of I_{Nap} in $V1^R$ that

482 cannot generate repetitive spiking (SS-$V1^R$) with $V1^R$ that can generate repetitive spiking

483 (RS-$V1^R$) and with $V1^R$ generating plateau potentials (PP-$V1^R$). We developed a voltage- and

484 current-clamp recording protocol in a given neuron allowing us to associate the amplitude of

485 the I_{Nap} with the excitability pattern in each type of spinal neuron (K-methanesulfonate

486 intracellular solution) (Figure 9 A1-A4). The same voltage ramp (70 mV/s) was used as

487 described above. The I_{Nap} current was revealed by subtracting ramp-evoked current in the

488 presence of 1 µM TTX from controls. In these conditions, SS-$V1^R$ had a significantly lower

489 g_{NaP} density (22.1 ± 12.6 pS/pF, n = 13) when compared to RS-$V1^R$ (57.8 ± 17.4 pS/pF, n = 7)

490 and to PP-$V1^R$ (70.6 ± 34.0 pS/pF, n = 11; $P < 0.0001$) (Figure 9A4). These results highlight a

491 direct relationship between the strength of I_{Nap} and the ability of $V1^R$ to sustain repetitive

492 spiking and plateau potential activity.

493   To determine whether I_{Nap} is required for repetitive spiking in embryonic $V1^R$, we

494   assessed the effect of riluzole on $V1^R$ that can sustain AP firing or plateau potential activity.

495   The application of 5 μM riluzole turned all RS-$V1^R$ into SS-$V1^R$ (n = 10) (Figure 9B). In the

496   presence of 5 μM riluzole, the depolarizing current step failed to trigger more than a doublet

497   in these cells. 5 μM riluzole did not significantly change the AP threshold (-37.2 ± 3.2 mV vs

498   -36.8 ± 6.0 mV with 5 μM riluzole, n = 10, P = 0.70). In all PP-$V1^R$, riluzole prevented the

499   plateau potential activity (n = 7) (Figure 9C). Increasing the amplitude of the injected current

500   failed to evoke any AP, indicating that PP-RCs were turned into non-excitable neurons when

501   I_{Nap} was blocked.

502   Altogether, these results indicate that I_{Nap} already plays an important role in $V1^R$

503   intrinsic activation properties at this early embryonic developmental stage of SC neuronal

504   networks.

505

506   ***Blocking persistent sodium current alters SNA pattern and SNA propagation along the***

507   ***cord.***

508   Synchronous activation of MNs and INs was proposed to drive episodes of activity

509   during SNA (Hanson and Landmesser, 2003; Czarnecki et al., 2014). If intrinsic activation

510   properties of the few INs that produce GABA including $V1^R$, rely on the I_{NaP}, we expected

511   that blocking I_{NaP} would alter episodes of activity during SNA in a manner similar to that

512   observed in the presence of $GABA_AR$ antagonists (Hanson and Landmesser, 2003; Czarnecki

513   et al., 2014). Blocking GABA neurotransmission during SNA evoked an increase in inter-

514   episode interval, but had little effect on the duration of episode of activity and on their

515   propagation along the cord (Hanson and Landmesser, 2003). In addition, we previously

516   showed that blocking GABA neurotransmission decreased the amplitude of spontaneous giant

517   inward currents (sGICs) recorded in MNs during SNA (Czarnecki et al., 2014).

518   To determine the involvement of I_{Nap} in SNA, we first tested the effect of 5 μM riluzole

519 on the spontaneous activity of MNs using whole-cell voltage-clamp recordings. In control

520 conditions, $_S$GICs occurred every 4 minutes (4.0 ± 0.8 min, n = 9), had mean amplitude of

521 291 ± 200 pA (n= 9) and a half-width of 0.6 ± 0.3 s (Vh = -60 mV; ECl = 3 mV) (Figure

522 10A1-A2). The time course of the effect of riluzole on sGIC occurrence was variable among

523 MNs. In one out of nine recorded MNs, riluzole abolished GIC activity in less than 10 min. In

524 other MNs, 1 to 2 GICs could still be observed during the 20- to 30-min application of

525 riluzole. (Figure 10A2). During this transitory period, riluzole significantly reduced the

526 amplitude of GICs (30.8 ± 32.7% reduction; n= 8; P = 0.039) (Figure 10B1) and the half-

527 duration of GICs (44.0 ± 27.2% reduction; n= 8; P = 0.0078) (Figure 10B2). In order to assess

528 the effect of riluzole on SNA, we made long-lasting extracellular recordings of SC activity

529 using two electrodes positioned on the cervical and lumbar superficial part of the ventral horn

530 of the SC at E12.5 (Czarnecki et al., 2014) (Figure 10C1).

531   These recordings allowed us to monitor SC neuron activity related to GIC activity

532 recorded in MNs (Czarnecki et al., 2014). We found that a 30- to 40-min application of 5 μM

533 riluzole significantly increased the inter-episode interval from 4.18 ± 1.93 min in control

534 conditions to 12.34 ± 9.08 min in the presence of riluzole (P < 0.001, n = 12 paired SCs)

535 (196.3 ± 203% increase) (Figure 10C2-C3), revealing a strong involvement of the I_{Nap} current

536 in the rhythmicity of early SC network activity. We therefore analyzed individual bursts of

537 AP exhibited by the cervical (C) and lumbar (L) SC networks in the presence of riluzole. We

538 found that the duration of bursts (both C and L), compared before (2.31 ± 0.89 s) and after the

539 riluzole application (1.44 ± 0.7 s), was significantly reduced (36.5 ± 18.3% reduction; n = 22;

540 P < 0.001) (Figure 10C4). In addition, the instantaneous AP frequency within a burst at both

541 the cervical level (C level) and the lumbar level (L level) was significantly reduced by 25.3 ±

542 11.9% (P < 0.001) in the presence of riluzole (112.4 ± 39.6 Hz in control conditions and 83.3

543 ± 34.4 Hz with riluzole, n = 22) (Figure 10C5). We also observed a reduction in the speed of

544 propagation of SNA episodes between the C level and L level of the SC in the presence of

545   riluzole. Propagation of SNA along the cord was investigated by analysis of the time needed

546   for a burst of AP recorded at the C level to reach L level (distance between the two recording

547   levels ≈ 4mm) (Yvert et al., 2004). We found that the C-L time was significantly increased (P

548   < 0.001) from 1.56 ± 0.42 s in control conditions to 2.42 ± 0.77 s in the presence of riluzole

549   ($56.3 \pm 36.1\%$ increase; n = 10) (Figure 10C6).

550   Riluzole had a stronger effect on SNA than previously observed in the presence of

551     $GABA_A R$ antagonists (Hanson and Landmesser, 2003; Czarnecki et al., 2014). Targeted

552   networks during extracellular recordings likely include MNs as well as surrounding INs

553   (Hanson and Landmesser, 2003; Czarnecki et al., 2014) including V1^R GABAergic INs.

554   Because most GABAergic V1^R are able to generate repetitive firing in response to GDP,

555   which is not the case for MNs (Czarnecki et al., 2014), this apparent discrepancy could be

556   explained if blocking GABA neurotransmission does not strongly alter GABAergic INs

557   firing, just as riluzole does. We cannot, however, exclude that I_{Nap} is also present in neurons

558   other than V1^R in the SC at E12.5. Anyhow, these results indicate that I_{Nap} plays an important

559   role in SNA at the onset of synaptogenesis (E12.5) by regulating neuron excitability in the

560   mouse embryonic SC.

561　**DISCUSSION**

562　　　　How excitability of neurons evolves during SC development was extensively studied at

563　developmental stages at which central pattern generators are already functional. At these

564　developmental stages (P0 to P5, postnatal day), I_{Nap} is present in MNs and in SC INs (Tazerart

565　et al., 2007; Zhong et al., 2007) and is required to generate fictive locomotion (Zhong et al.,

566　2007). Here, we show that $V1^R$ already express I_{Nap} at the onset of synaptogenesis in the

567　embryonic (E12.5) SC (Scain et al., 2010). Our results reveal that I_{Nap} already closely controls

568　the $V1^R$ excitability pattern. In addition, we found that low concentrations of riluzole, an I_{Nap}

569　blocker, dramatically altered the SC SNA pattern, suggesting that I_{Nap} is already expressed by

570　neurons in the mammalian embryonic SC well before the control of muscle contraction by

571　MNs (Sanes and Lichtman, 1999)**.**

572

573　*$V1^R$ display different excitability patterns at the onset of SNA.*

574　　　　Repetitive firing of presynaptic neurons is required for long-lasting neurotransmitter-

575　dependent episodes, as GDPs observed in MNs at E12.5. Previous studies have examined the

576　development of passive and active membrane properties of MNs and INs in late embryonic

577　and newborn rats or mice (Ziskind-Conhaim, 1988; Gao and Ziskind-Conhaim, 1998; Vinay

578　et al., 2000; Theiss et al., 2007; Perry et al., 2015; Bikoff et al., 2016), but there is no

579　information about the excitability of INs at early mammalian embryonic developmental stages

580　when SNA first arises. We found that a majority of $V1^R$ ($\approx$ 60%) can already generate

581　repetitive AP firing or long-lasting sodium-dependent plateau potentials at the onset of SNA,

582　indicating that these cells are already active at this early embryonic developmental stage. Our

583　analysis revealed a strong heterogeneity in $V1^R$ excitability pattern, which can be separated

584　into different independent classes, but such functional diversity is unlikely to persist in the

585　adult. In the adult, $V1^R$ were found to generate two different excitability patterns only, a

586　prominent low-threshold depolarization and burst firing followed by continuous firing

587 dependent on Vh (Perry et al., 2015; Bikoff et al., 2016). It is therefore likely that the

588 functional heterogeneity we observed at E12.5 reflects an immature form of $V1^R$ excitability

589 (Perry et al., 2015; Bikoff et al., 2016). Sodium-dependent plateau potentials were also

590 observed in ipsilateral caudal SC INs of zebrafish embryos at the appearance of functional

591 neuromuscular junctions and then disappeared at more mature stages (Tong and McDearmid,

592 2012).

593

594 *I_{Nap} already regulate excitability patterns of $V1^R$ at early developmental stages.*

595   In this study, we reveal the presence of I_{Nap} in neurons of mammalian embryos at the

596 onset of SNA. Persistent inward currents (PICs) are present in many types of neurons. PICs

597 can be calcium- and/or sodium-dependent depending on the neuron subtypes. We did not find

598 any evidence for a significant calcium component in recorded PICs in $V1^R$ at E12.5. Indeed,

599 the PIC was fully blocked by TTX in $V1^R$, which contrasts with what is known about more

600 mature spinal neurons like MNs (Hounsgaard and Kiehn, 1989; Bui et al., 2006; Carlin et al.,

601 2009). Accordingly, we concluded that immature $V1^R$ at the onset of SNA generate a pure

602 sodium-dependent PIC. I_{Nap} recorded in $V1^R$ of the mouse embryo has an activation onset ($\approx$ -

603 65 mV) similar to that of I_{Nap} at postnatal developmental stages in the rat and mouse SC (Kuo

604 et al., 2006; Tazerart et al., 2007; Theiss et al., 2007; Tazerart et al., 2008; Dai and Jordan,

605 2010). The Boltzmann constant of activation calculated for I_{Nap} in $V1^R$ ($\approx$ 7 mV) is in the

606 range of the values known for I_{Nap} in INs and MNs ($\approx$ 6 mV) of neonatal rats (Bouhadfane et

607 al., 2013) or in the calyx of Held ($\approx$ 8 mV) (Huang and Trussell, 2008). Small differences in

608 the voltage dependency of I_{Nap} activation may reflect differences in sodium channel α-subunit

609 and/or β-subunit combination expression (Isom et al., 1994; Qu et al., 2001).

610   I_{Nap} likely has diverse functions and plays an important function in locomotor pattern

611 generation in neonatal rats (Tazerart, S*., et al.* 2007). In neonate SC, I_{Nap} is present in both

612 INs and MNs (Kuo et al., 2006; Tazerart et al., 2007) and is known to generate pacemaker

613   activities in central pattern generator INs (Tazerart et al., 2008). Remarkably, I_{Nap} also

614   contributes to lumbar MN activity related to plateau potential in rat neonates (Bouhadfane et

615   al., 2013). However, while in neonate MNs, I_{Nap} is essential for self-sustained firing only

616   during calcium-dependent plateau potential depolarization (Carlin et al., 2009; Bouhadfane et

617   al., 2013), plateau potential activity in V1^R at E12.5.is fully I_{Nap}-dependent

618

619   ***Does I_{Nap} already participate in SC activity at the onset of neuronal network formation?***

620   I_{Nap} plays a crucial role in the regulation of locomotor pattern generation in rat

621   neonates (Tazerart et al., 2007; Zhong et al., 2007; Bouhadfane et al., 2013) and in the SC of

622   the zebrafish embryo during the cooling stage (Tong and McDearmid, 2012). Here, we

623   demonstrated that a low concentration of riluzole dramatically reduced the amplitude and the

624   duration of GICs recorded on MNs and strongly altered SC activity (extracellular recordings)

625   at the onset of SNA.

626   In our experiments, we used a concentration of riluzole that has a minimal effect on the

627   sodium AP waveform (Figure 6). However, beside its effect on $I_{Nap,}$ riluzole is known to

628   inhibit the release of glutamate (Cheramy et al., 1992), to inhibit AMPA receptor activation

629   (Albo et al., 2004), GABA$_A$ and glycine receptor activation (Mohammadi et al., 2001) and to

630   block several voltage-gated channels including calcium channels (Huang et al., 1997; Ahn et

631   al., 2006). With the exception of AMPA receptor inhibition (Albo et al., 2004), these side

632   effects of riluzole occur at concentrations ≥ 10 μM (Cheramy et al., 1992; Huang et al., 1997;

633   Mohammadi et al., 2001; Ahn et al., 2006). Because the inhibition of glutamate

634   neurotransmission did not alter SNA in the mouse embryonic SC at E12.5 (Czarnecki et al.,

635   2014), it is unlikely that the alteration of SNA we observed in the presence of 5 μM riluzole is

636   caused by the inhibition of glutamatergic synaptic activity (Albo et al., 2004). Accordingly,

637   we propose that I_{Nap} already regulates the SNA pattern at the onset of synaptogenesis in

638   mammalian embryos before the formation of the locomotor SC network and of functional

639 neuromuscular junctions. However, we cannot exclude that spinal neurons other than $V1^R$

640 exhibit I_{Nap} dependent sustain discharge at this developmental stage.

641   Because $V1^R$ already produce GABA at E12.5 and make synaptic-like contacts with

642 MNs while MNs make synaptic-like contacts with $V1^R$ (see also (Alvarez et al., 2013), it is

643 likely that $V1^R$ participate in early SC SNA. Although correlative, our data reinforce the

644 hypothesis that a primitive $V1^R$-MN recurrent-like circuit may exist at the onset of

645 synaptogenesis in the mouse embryo. This primitive $V1^R$-MN recurrent circuit differs in

646 several ways from the adult RC-MN recurrent circuits. Evoked MN spiking did not trigger a

647 recurrent synaptic response at E12.5 (Le Bras et al., 2014), which suggests that although $V1^R$

648 projects on MNs and vice versa, it is unlikely that $V1^R$ projecting on MNs receive inputs from

649 these MNs and vice versa. It is also unlikely that MN release sites apposed on $V1^R$ are mixed

650 glutamatergic and cholinergic inputs as observed at postnatal stages (Nishimaru et al., 2005;

651 Lamotte d'Incamps et al., 2017). Glutamatergic vesicular transporters were not observed

652 within MNs at E12.5 (Czarnecki et al., 2014). But we cannot completely exclude that some

653 immature motor axon synapses on $V1^R$ already release aspartate, as suggested in the adult

654 (Richards et al., 2014). However, contrary to what is observed for GABAergic and

655 cholinergic networks, the spontaneous activation of glutamate receptors had a minor role only

656 in the generation of SNA episodes at E12.5 (Czarnecki et al., 2014).

657   We clearly show that paracrine release of GABA can occur in the embryonic SC, which

658 may explain the smooth shape of GABAergic-dependent GDPs observed in MNs during SNA

659 (Czarnecki et al., 2014). Since $V1^R$ are GABAergic at this embryonic age and possess

660 putative release sites, $V1^R$ may be one of the sources for the paracrine release of GABA we

661 observed. Accordingly, we propose that $V1^R$-MN interactions occur through synaptic and

662 paracrine release and participate in the synchronization of neuronal assembly required for the

663 generation of the propagating waves of activity characterizing SC SNA at E12.5 (Momose-

664 Sato and Sato, 2013).

665

Conclusions

666

667 Taken together, our findings demonstrate that I_{Nap} is already present in developing SC

668 neurons at an early developmental stage and governs $V1^R$ excitability. I_{Nap} plays an important

669 role in the regulation of locomotor pattern generation at postnatal developmental stages in

670 rodents (Tazerart et al., 2008). Because the application of a low concentration of riluzole

671 altered SNA, we propose that I_{Nap} contributes to the patterning of embryonic SC activity at the

672 onset of synaptogenesis. Accordingly, the capacity of SC neurons to generate sustained firing

673 must be crucial for correct embryonic SC patterned activity at the onset of synaptogenesis,

674 which is required for the correct development of MN projections toward their peripheral

675 targets (Hanson and Landmesser, 2006).

676

677   **BIBLIOGRAPHY**

678   Ahn HS, Kim SE, Jang HJ, Kim MJ, Rhie DJ, Yoon SH, Jo YH, Kim MS, Sung KW, Hahn
679   SJ (2006) Interaction of riluzole with the closed inactivated state of Kv4.3 channels.
680   The Journal of pharmacology and experimental therapeutics 319:323-331.
681   Albo F, Pieri M, Zona C (2004) Modulation of AMPA receptors in spinal motor neurons by
682   the neuroprotective agent riluzole. Journal of neuroscience research 78:200-207.
683   Allain AE, Bairi A, Meyrand P, Branchereau P (2004) Ontogenic changes of the GABAergic
684   system in the embryonic mouse spinal cord. Brain research 1000:134-147.
685   Allain AE, Bairi A, Meyrand P, Branchereau P (2006) Expression of the glycinergic system
686   during the course of embryonic development in the mouse spinal cord and its co-
687   localization with GABA immunoreactivity. The Journal of comparative neurology
688   496:832-846.
689   Alvarez FJ, Benito-Gonzalez A, Siembab VC (2013) Principles of interneuron development
690   learned from Renshaw cells and the motoneuron recurrent inhibitory circuit. Annals of
691   the New York Academy of Sciences 1279:22-31.
692   Barberis A, Mozrzymas JW, Ortinski PI, Vicini S (2007) Desensitization and binding
693   properties determine distinct alpha1beta2gamma2 and alpha3beta2gamma2 GABA(A)
694   receptor-channel kinetic behavior. The European journal of neuroscience 25:2726-
695   2740.
696   Ben-Ari Y, Cherubini E, Corradetti R, Gaiarsa JL (1989) Giant synaptic potentials in
697   immature rat CA3 hippocampal neurones. J Physiol 416:303-325.
698   Benito-Gonzalez A, Alvarez FJ (2012) Renshaw cells and Ia inhibitory interneurons are
699   generated at different times from p1 progenitors and differentiate shortly after exiting
700   the cell cycle. J Neurosci 32:1156-1170.
701   Bikoff JB, Gabitto MI, Rivard AF, Drobac E, Machado TA, Miri A, Brenner-Morton S,
702   Famojure E, Diaz C, Alvarez FJ, Mentis GZ, Jessell TM (2016) Spinal Inhibitory
703   Interneuron Diversity Delineates Variant Motor Microcircuits. Cell 165:207-219.
704   Bouhadfane M, Tazerart S, Moqrich A, Vinay L, Brocard F (2013) Sodium-mediated plateau
705   potentials in lumbar motoneurons of neonatal rats. J Neurosci 33:15626-15641.
706   Bui TV, Ter-Mikaelian M, Bedrossian D, Rose PK (2006) Computational estimation of the
707   distribution of L-type Ca(2+) channels in motoneurons based on variable threshold of
708   activation of persistent inward currents. Journal of neurophysiology 95:225-241.
709   Carlin KP, Bui TV, Dai Y, Brownstone RM (2009) Staircase currents in motoneurons: insight
710   into the spatial arrangement of calcium channels in the dendritic tree. J Neurosci
711   29:5343-5353.
712   Carr PA, Alvarez FJ, Leman EA, Fyffe RE (1998) Calbindin D28k expression in
713   immunohistochemically identified Renshaw cells. Neuroreport 9:2657-2661.
714   Cheramy A, Barbeito L, Godeheu G, Glowinski J (1992) Riluzole inhibits the release of
715   glutamate in the caudate nucleus of the cat in vivo. Neuroscience letters 147:209-212.
716   Corlew R, Bosma MM, Moody WJ (2004) Spontaneous, synchronous electrical activity in
717   neonatal mouse cortical neurones. J Physiol 560:377-390.
718   Czarnecki A, Le Corronc H, Rigato C, Le Bras B, Couraud F, Scain AL, Allain AE, Mouffle
719   C, Bullier E, Mangin JM, Branchereau P, Legendre P (2014) Acetylcholine controls
720   GABA-, glutamate-, and glycine-dependent giant depolarizing potentials that govern
721   spontaneous motoneuron activity at the onset of synaptogenesis in the mouse
722   embryonic spinal cord. J Neurosci 34:6389-6404.
723   Dai Y, Jordan LM (2010) Multiple patterns and components of persistent inward current with
724   serotonergic modulation in locomotor activity-related neurons in Cfos-EGFP mice.
725   Journal of neurophysiology 103:1712-1727.

726 Delpy A, Allain AE, Meyrand P, Branchereau P (2008) NKCC1 cotransporter inactivation
727   underlies embryonic development of chloride-mediated inhibition in mouse spinal
728   motoneuron. J Physiol 586:1059-1075.
729 Dottori M, Gross MK, Labosky P, Goulding M (2001) The winged-helix transcription factor
730   Foxd3 suppresses interneuron differentiation and promotes neural crest cell fate.
731   Development 128:4127-4138.
732 Eccles JC, Fatt P, Landgren S (1956) The inhibitory pathway to motoneurones. Progress in
733   neurobiology:72-82.
734 Feller MB (1999) Spontaneous correlated activity in developing neural circuits. Neuron
735   22:653-656.
736 Gao BX, Ziskind-Conhaim L (1998) Development of ionic currents underlying changes in
737   action potential waveforms in rat spinal motoneurons. Journal of neurophysiology
738   80:3047-3061.
739 Garaschuk O, Hanse E, Konnerth A (1998) Developmental profile and synaptic origin of
740   early network oscillations in the CA1 region of rat neonatal hippocampus. J Physiol
741   507 (Pt 1):219-236.
742 Garaschuk O, Linn J, Eilers J, Konnerth A (2000) Large-scale oscillatory calcium waves in
743   the immature cortex. Nat Neurosci 3:452-459.
744 Geiman EJ, Knox MC, Alvarez FJ (2000) Postnatal maturation of gephyrin/glycine receptor
745   clusters on developing Renshaw cells. The Journal of comparative neurology 426:130-
746   142.
747 Gonzalez-Islas C, Wenner P (2006) Spontaneous network activity in the embryonic spinal
748   cord regulates AMPAergic and GABAergic synaptic strength. Neuron 49:563-575.
749 Gust J, Wright JJ, Pratt EB, Bosma MM (2003) Development of synchronized activity of
750   cranial motor neurons in the segmented embryonic mouse hindbrain. J Physiol
751   550:123-133.
752 Hanson MG, Landmesser LT (2003) Characterization of the circuits that generate
753   spontaneous episodes of activity in the early embryonic mouse spinal cord. J Neurosci
754   23:587-600.
755 Hanson MG, Landmesser LT (2006) Increasing the frequency of spontaneous rhythmic
756   activity disrupts pool-specific axon fasciculation and pathfinding of embryonic spinal
757   motoneurons. J Neurosci 26:12769-12780.
758 Hanson MG, Milner LD, Landmesser LT (2008) Spontaneous rhythmic activity in early chick
759   spinal cord influences distinct motor axon pathfinding decisions. Brain Res Rev
760   57:77-85.
761 Hounsgaard J, Kiehn O (1989) Serotonin-induced bistability of turtle motoneurones caused by
762   a nifedipine-sensitive calcium plateau potential. J Physiol 414:265-282.
763 Huang CS, Song JH, Nagata K, Yeh JZ, Narahashi T (1997) Effects of the neuroprotective
764   agent riluzole on the high voltage-activated calcium channels of rat dorsal root
765   ganglion neurons. The Journal of pharmacology and experimental therapeutics
766   282:1280-1290.
767 Huang H, Trussell LO (2008) Control of presynaptic function by a persistent Na(+) current.
768   Neuron 60:975-979.
769 Isom LL, De Jongh KS, Catterall WA (1994) Auxiliary subunits of voltage-gated ion
770   channels. Neuron 12:1183-1194.
771 Kirkby LA, Sack GS, Firl A, Feller MB (2013) A role for correlated spontaneous activity in
772   the assembly of neural circuits. Neuron 80:1129-1144.
773 Kuo JJ, Lee RH, Zhang L, Heckman CJ (2006) Essential role of the persistent sodium current
774   in spike initiation during slowly rising inputs in mouse spinal neurones. J Physiol
775   574:819-834.

776 Lamotte d'Incamps B, Bhumbra GS, Foster JD, Beato M, Ascher P (2017) Segregation of
777   glutamatergic and cholinergic transmission at the mixed motoneuron Renshaw cell
778   synapse. Scientific reports 7:4037.
779 Landmesser LT, O'Donovan MJ (1984) Activation patterns of embryonic chick hind limb
780   muscles recorded in ovo and in an isolated spinal cord preparation. J Physiol 347:189-
781   204.
782 Le Bras B, Freal A, Czarnecki A, Legendre P, Bullier E, Komada M, Brophy PJ, Davenne M,
783   Couraud F (2014) In vivo assembly of the axon initial segment in motor neurons.
784   Brain structure & function 219:1433-1450.
785 Le-Corronc H, Rigo JM, Branchereau P, Legendre P (2011) GABA(A) receptor and glycine
786   receptor activation by paracrine/autocrine release of endogenous agonists: more than a
787   simple communication pathway. Molecular neurobiology 44:28-52.
788 Lee RH, Heckman CJ (1998) Bistability in spinal motoneurons in vivo: systematic variations
789   in persistent inward currents. Journal of neurophysiology 80:583-593.
790 Marder E, Rehm KJ (2005) Development of central pattern generating circuits. Curr Opin
791   Neurobiol 15:86-93.
792 Mohammadi B, Krampfl K, Moschref H, Dengler R, Bufler J (2001) Interaction of the
793   neuroprotective drug riluzole with GABA(A) and glycine receptor channels. European
794   journal of pharmacology 415:135-140.
795 Momose-Sato Y, Sato K (2013) Optical imaging of the spontaneous depolarization wave in
796   the mouse embryo: origins and pharmacological nature. Annals of the New York
797   Academy of Sciences 1279:60-70.
798 Moody WJ (1998) Control of spontaneous activity during development. Journal of
799   neurobiology 37:97-109.
800 Muller A, Kukley M, Stausberg P, Beck H, Muller W, Dietrich D (2005) Endogenous Ca2+
801   buffer concentration and Ca2+ microdomains in hippocampal neurons. J Neurosci
802   25:558-565.
803 Myers CP, Lewcock JW, Hanson MG, Gosgnach S, Aimone JB, Gage FH, Lee KF,
804   Landmesser LT, Pfaff SL (2005) Cholinergic input is required during embryonic
805   development to mediate proper assembly of spinal locomotor circuits. Neuron 46:37-
806   49.
807 Nishimaru H, Restrepo CE, Ryge J, Yanagawa Y, Kiehn O (2005) Mammalian motor neurons
808   corelease glutamate and acetylcholine at central synapses. Proceedings of the National
809   Academy of Sciences of the United States of America 102:5245-5249.
810 Perry S, Gezelius H, Larhammar M, Hilscher MM, Lamotte d'Incamps B, Leao KE,
811   Kullander K (2015) Firing properties of Renshaw cells defined by Chrna2 are
812   modulated by hyperpolarizing and small conductance ion currents Ih and ISK. The
813   European journal of neuroscience 41:889-900.
814 Prasad T, Wang X, Gray PA, Weiner JA (2008) A differential developmental pattern of spinal
815   interneuron apoptosis during synaptogenesis: insights from genetic analyses of the
816   protocadherin-gamma gene cluster. Development 135:4153-4164.
817 Qu Y, Curtis R, Lawson D, Gilbride K, Ge P, DiStefano PS, Silos-Santiago I, Catterall WA,
818   Scheuer T (2001) Differential modulation of sodium channel gating and persistent
819   sodium currents by the beta1, beta2, and beta3 subunits. Molecular and cellular
820   neurosciences 18:570-580.
821 Richards DS, Griffith RW, Romer SH, Alvarez FJ (2014) Motor axon synapses on renshaw
822   cells contain higher levels of aspartate than glutamate. PloS one 9:e97240.
823 Rockhill W, Kirkman JL, Bosma MM (2009) Spontaneous activity in the developing mouse
824   midbrain driven by an external pacemaker. Dev Neurobiol 69:689-704.
825 Safiulina VF, Cherubini E (2009) At immature mossy fibers-CA3 connections, activation of
826   presynaptic GABA(B) receptors by endogenously released GABA contributes to
827   synapses silencing. Frontiers in cellular neuroscience 3:1.

828 Sanes JR, Lichtman JW (1999) Development of the vertebrate neuromuscular junction.
829   Annual review of neuroscience 22:389-442.
830 Sapir T, Geiman EJ, Wang Z, Velasquez T, Mitsui S, Yoshihara Y, Frank E, Alvarez FJ,
831   Goulding M (2004) Pax6 and engrailed 1 regulate two distinct aspects of renshaw cell
832   development. J Neurosci 24:1255-1264.
833 Scain AL, Le Corronc H, Allain AE, Muller E, Rigo JM, Meyrand P, Branchereau P,
834   Legendre P (2010) Glycine release from radial cells modulates the spontaneous
835   activity and its propagation during early spinal cord development. J Neurosci 30:390-
836   403.
837 Stam FJ, Hendricks TJ, Zhang J, Geiman EJ, Francius C, Labosky PA, Clotman F, Goulding
838   M (2012) Renshaw cell interneuron specialization is controlled by a temporally
839   restricted transcription factor program. Development 139:179-190.
840 Tamamaki N, Yanagawa Y, Tomioka R, Miyazaki J, Obata K, Kaneko T (2003) Green
841   fluorescent protein expression and colocalization with calretinin, parvalbumin, and
842   somatostatin in the GAD67-GFP knock-in mouse. The Journal of comparative
843   neurology 467:60-79.
844 Tazerart S, Vinay L, Brocard F (2008) The persistent sodium current generates pacemaker
845   activities in the central pattern generator for locomotion and regulates the locomotor
846   rhythm. J Neurosci 28:8577-8589.
847 Tazerart S, Viemari JC, Darbon P, Vinay L, Brocard F (2007) Contribution of persistent
848   sodium current to locomotor pattern generation in neonatal rats. Journal of
849   neurophysiology 98:613-628.
850 Theiss RD, Kuo JJ, Heckman CJ (2007) Persistent inward currents in rat ventral horn
851   neurones. J Physiol 580:507-522.
852 Tong H, McDearmid JR (2012) Pacemaker and plateau potentials shape output of a
853   developing locomotor network. Current biology : CB 22:2285-2293.
854 Urbani A, Belluzzi O (2000) Riluzole inhibits the persistent sodium current in mammalian
855   CNS neurons. The European journal of neuroscience 12:3567-3574.
856 Vinay L, Brocard F, Pflieger JF, Simeoni-Alias J, Clarac F (2000) Perinatal development of
857   lumbar motoneurons and their inputs in the rat. Brain research bulletin 53:635-647.
858 Watt AJ, Cuntz H, Mori M, Nusser Z, Sjostrom PJ, Hausser M (2009) Traveling waves in
859   developing cerebellar cortex mediated by asymmetrical Purkinje cell connectivity. Nat
860   Neurosci 12:463-473.
861 Wenner P, O'Donovan MJ (2001) Mechanisms that initiate spontaneous network activity in
862   the developing chick spinal cord. Journal of neurophysiology 86:1481-1498.
863 Wichterle H, Lieberam I, Porter JA, Jessell TM (2002) Directed differentiation of embryonic
864   stem cells into motor neurons. Cell 110:385-397.
865 Young SH, Poo MM (1983) Spontaneous release of transmitter from growth cones of
866   embryonic neurones. Nature 305:634-637.
867 Yvert B, Branchereau P, Meyrand P (2004) Multiple spontaneous rhythmic activity patterns
868   generated by the embryonic mouse spinal cord occur within a specific developmental
869   time window. Journal of neurophysiology 91:2101-2109.
870 Zhang LI, Poo MM (2001) Electrical activity and development of neural circuits. Nat
871   Neurosci 4 Suppl:1207-1214.
872 Zhong G, Masino MA, Harris-Warrick RM (2007) Persistent sodium currents participate in
873   fictive locomotion generation in neonatal mouse spinal cord. J Neurosci 27:4507-
874   4518.
875 Ziskind-Conhaim L (1988) Electrical properties of motoneurons in the spinal cord of rat
876   embryos. Developmental biology 128:21-29.
877 Ziskind-Conhaim L, Wu L, Wiesner EP (2008) Persistent sodium current contributes to
878   induced voltage oscillations in locomotor-related hb9 interneurons in the mouse spinal
879   cord. Journal of neurophysiology 100:2254-2264.

880
881   **LEGENDS**

882   *Figure 1: V1^R identification in the lumbar spinal cord of E12.5 embryos*

883   A) Coronal slice of the lumbar spinal cord of E12.5 GA67-eGFP mouse embryo showing the

884   distribution of eGFP neurons (A1), FoxD3 (A2) and calbindin (A3) immunoreactive neurons.

885   A4) Superimposed images showing the colocalization of eGFP, FoxD3 immunostaining and

886   calbindin immunostaining. B) Enlarged images from A showing that eGFP neurons localized

887   in the ventrolateral area of the spinal cord (B1) are Foxd3 immunoreactive (B2), most of them

888   being calbindin immunoreactive (B3-B4). C) Coronal slice of the ventrolateral part of the

889   lumbar spinal cord of E12.5 GA67-eGFP mouse embryo showing the distribution of eGFP

890   neurons (C1), FoxD3 (C2) and MafB (C3) immunoreactive neurons. C4) Superimposed

891   images showing the colocalization of eGFP FoxD3 immunostaining and MafB

892   immunostaining. Note that all FoxD3 immunoreactive neurons localized in the marginal zone

893   of the ventrolateral area are also MafB-positive, indicating that they are V1^R neurons. D1)

894   Example of a neuron filled with neurobiotin during the recording at the lumbar level of an

895   embryonic spinal cord open book preparation of GAD67-GFP mice at E12.5. This eGFP

896   neuron (D2) was immunoreactive to Foxd3 antibody (D3), as shown in the merged images

897   (D4). Each image corresponds to a single confocal section.

898

899   *Figure 2: V1^R already produce GABA in the lumbar spinal cord of E12.5 embryos*

900   A) Single confocal sections of coronal slice of the lumbar spinal cord of E12.5 GA67-eGFP

901   mouse embryo showing the distribution of eGFP neurons (A1), calbindin (A2) and GABA

902   (A3) immunoreactive neurons. A4) Superimposed images showing the colocalization of

903   eGFP, calbindin immunostaining and GABA immunostaining. B1-B3) Enlarged images from

904   A1, A2 and A3 showing eGFP neurons (B1), calbindin immunoreactive neurons (B2), and

905   GABA immunoreactive neurons (B3) in the ventrolateral area of the spinal cord. B4)

906   Superimposed images showing the colocalization of calbindin immunostaining and GABA

907   immunostaining with z projections within a stack. Note the colocalization of calbindin

908   immunostaining and GABA immunostaining in the three axes, indicating that $V1^R$ already

909   produce GABA at E12.5.

910

911   *Figure 3: $V1^R$ make synaptic-like contacts with motoneurons (HB9-eGFP) at E12.5.*

912   A) Coronal slice of the lumbar spinal cord of E12.5 HB9-eGFP mouse embryo with cell

913   nucleus staining (Hoesch) and synaptophysin immunostaining (A1). A1) Note that

914   synaptophysin immunostaining is mainly restricted in the ventral funiculus (VF) A2)

915   Calbindin staining showing the distribution of $V1^R$ neurite extensions and synaptophysin

916   immunostaining. A3) eGFP immunostaining showing the distribution of MN neurite

917   extensions and synaptophysin immunostaining. Antibody against GFP was used to visualize

918   MN morphology better (Czarnecki et al., 2014). A4) Superimposition of eGFP fluorescence,

919   calbindin immunostaining and synaptophysin immunostaining (A1, A2, A3, and A4 are

920   confocal stacks). B) Single confocal sections with z projections of enlarged images from A2,

921   A3 and A4 showing the colocalization of synaptophysin punctates with calbindin

922   immunostaining apposed to eGFP immunostaining (B1, B2 and B3; enlarged images in

923   boxes). B2) Note that a synaptophysin punctate colocalized with calbindin immunostaining

924   (B1, arrow) did not colocalize with eGFP immunostaining (B2, arrow). Note that

925   synaptophysin punctate colocalized with eGFP immunostaining (B1, arrow heads) did not

926   colocalize with calbindin immunostaining (B2, arrow head). Barred arrow (B1) shows a

927   colocalization of calbindin and synaptophysin immunostaining not apposed to eGFP

928   immunostaining. B4) superimposed images (B1, B2 and B3) with z projections showing

929   calbindin immunostaining and eGFP appositions. C1) Confocal stacks showing neurobiotin

930   injected Foxd3 immunoreactive $V1^R$, HB9-eGFP immunostaining and synaptophysin

931   immunostaining in an SC open book preparation. C2-C4). Single confocal sections with z

932   projections of enlarged images from C1 (white box) showing the colocalization of

933 synaptophysin punctates with neurobiotin staining (C2), the apposition of the same

934 synaptophysin punctates to eGFP (C3) and the apposition of neurobiotin staining containing

935 synaptophysin punctates to eGFP (C4) (enlarged image in boxes in C2, C3 and C4),

936 indicating the presence of a $V1^R$ synaptic-like contact on an MN neurite.

937

938 *Figure 4: Paracrine release of GABA detected by a sniffer outside-out patch.*

939 A1) Upper drawing showing the location of the outside-out sniffer to detect paracrine release

940 of GABA (left) and to obtain outside-out currents in response to GABA application (left).

941 Lower traces (purple): example of outside-out sniffer current evoked by the application of 30

942 mM KCl when the sniffer electrode was positioned in the dorsal area of the SC close to motor

943 columns. Enlarged trace shows single channel currents at the onset of the sniffer current.

944 Right traces (green) show outside-out current evoked by the application of 3 μM and 10 μM

945 GABA to a sniffer patch positioned outside the spinal cord. Purple and green traces are from

946 the same outside-out patch. A2) Box plots of normalized maximum outside-out current

947 evoked by KCl application (purple left) and by the application of 3 μM or 10 μM GABA

948 (green right) on the same outside-out sniffer patch (n = 9). Amplitudes of the outside-out

949 currents evoked by the application of 30 mM KCl, 3 μM or 10 μM GABA, were normalized

950 to the amplitude of the outside-out currents evoked by the application of 30 μM GABA (not

951 shown). Note that the normalized amplitude of the outside-out current evoked by 30 mM KCl

952 application (0.118 ± 0.097) was not significantly different (P > 0.9) from the normalized

953 amplitude of the outside-out current evoked by the application of 3 μM GABA (0.152 ±

954 0.062). Normalized amplitudes of the outside-out currents evoked by the application of 30

955 mM KCl or of 3 μM GABA were significantly different (KCl: *P* = 0.0029; 3 μM GABA: *P* =

956 0.00665) from the normalized amplitude of the outside-out currents evoked by the application

957 of 10 μM GABA (0.697 ± 0.073). $V1^R$: immature Renshaw cell; MN: motoneuron; ** *P* <

958 0.01. B1) Example of motoneuron membrane potential depolarization evoked by the

959   application of 3 μM GABA in the presence of 1 μM TTX (current clamp recording: Vh = -60

960   mV; ECl = - 30 mV). The application of 3 μM GABA evoked a depolarizing response of 20.6

961   ± 6.1 mV (n = 7).

962

963   *Figure 5: V1^R display plateau potential, repetitive firing or generate a single action*

964   *potential during episodes of SNA in E12.5 spinal cord.*

965   Examples of spontaneous activities recorded in V1^R being characterized by GDPs displaying

966   plateau potential (A), repetitive firing (B) or a single action potential (C) activity (V holding =

967   -60 mV). Recordings shown in A, B and C are from different cells.

968

969   *Figure 6: V1^R display different excitability patterns in E12.5 embryonic spinal cords.*

970   Excitability patterns were analyzed using depolarizing current step (2 sec) and depolarizing

971   current ramp (20 sec). A-D) Representative traces of voltage responses showing single-

972   spiking activity (A), plateau potential activity (B) repetitive AP firing (C) and mixed

973   repetitive-spiking/plateau potential activity (D). E) Proportions of V1^R subtypes according to

974   the observed discharge patterns. 28.6% of V1^R could not sustain repetitive spiking, 41.7%

975   were repetitive-spiking V1^R, 8.5% were mixed V1^R, 21.2% were plateau potential V1^R (n =

976   164). F) Plateau potentials are blocked by TTX (1 μM) application (n = 5/5) (F1, F2). F2)

977   Plateau potentials are evoked by short (100 ms) pulses of depolarizing current.

978

979   *Figure 7: Persistent sodium current (I$_{Nap}$) is already expressed in V1^R*

980   A1) Representative trace of I$_{Nap}$ evoked by a slow depolarizing voltage ramp in a V1^R (CsCl

981   intracellular solution). I$_{Nap}$ (black trace) was isolated by subtracting the current elicited by a

982   voltage ramp (70 mV/s) in the presence of TTX (insert green trace) from the control current

983   (insert black trace). TTX-sensitive current was blocked by 5 μM riluzole (red trace). Left

984   insert shows the protocol to generate voltage-dependent slow inward currents in control

985   conditions (black), after 5 µM riluzole application (red) or 1 µM TTX application (green).

986   Right insert shows the current evoked by a depolarizing voltage step from -100 mV to 20 mV

987   in the absence and in the presence of 5 µM riluzole. A2) Voltage dependence of I_{Nap}

988   conductance calculated from the trace shown in A1. The activation curve was obtained by

989   transforming the current evoked by a depolarizing voltage ramp from -100 mV to 20 mV (70

990   mV/s) using the following equation: $G_{NaP} = -I_{Nap}/((-Vh)+E_{Na}+)$ where Vh is the holding

991   potential at time t during a depolarizing voltage ramp and $E_{Na}+$ is the equilibrium potential for

992   sodium ($E_{Na}+ = 60$ mV). The G_{NaP}/Vh curve was fitted with a Boltzmann function (see

993   methods), where V_{half} is the Vh value for I_{Nap} half activation, k the slope factor of the curve

994   and G_{max} the maximum conductance. B) Box plot showing G_{max} density in RCs (n=12). C)

995   Box plots showing the variation of the % I_{Nap} block by 5 µM riluzole in RC.

996

997   ***Figure 8: Effect of 5 and 10 µM riluzole on action potentials.***

998   A) Effect of 5 µM (red trace) and 10 µM (blue trace) riluzole on the action potential (AP)

999   evoked by a depolarizing current step in an MN. B1) Box plot showing the % changes in AP

1000   amplitude (% of control) in the presence of 5 µM riluzole and 10 µM riluzole. B2) Box plot

1001   showing the % changes in AP threshold (% of control) in the presence of 5 µM and 10 µM

1002   riluzole. B3) Box plot showing the % changes in AP half-width (% of control) in the presence

1003   of 5 µM and 10 µM riluzole.

1004

1005   ***Figure 9: Sustained discharge in embryonic V1^R depends on persistent sodium current***

1006   ***(I_{Nap}).***

1007   A) Representative traces of I_{Nap} recorded in V1^R that cannot sustain repetitive spiking (SS-

1008   V1^R) (A1), in a repetitive-spiking V1^R (RS-V1^R) (A2) and in a plateau potential V1^R (PP-

1009   V1^R) (A3). I_{Nap} was isolated by subtracting the current elicited by a slow voltage ramp (-100

1010   to + 20 mV; 70 mV/s) in the presence of 1 µM TTX from the current evoked in the absence of

1011 TTX. A4) Box plots showing Gmax density in SS-V1^R (n=13), RS-RCs (n=8) and PP-V1^R (n

1012 = 11). Note that Gmax density is significantly lower in SS-V1^R (p <0.01). B) Representative

1013 traces showing the effect of riluzole application (5 µM) on the intrinsic activity pattern

1014 evoked by suprathreshold current steps (left traces) or a suprathreshold current ramp (right

1015 traces) in an RS-V1^R. Note that riluzole blocks repetitive spiking (n= 10/10). C)

1016 Representative traces showing the effect of riluzole application on plateau potential evoked by

1017 suprathreshold current steps (left traces) or by a suprathreshold current ramp (right traces) in a

1018 V1^R. Note that riluzole blocks plateau potential activity (n=7/7).

1019

1020 **_Figure 10: Riluzole dramatically decreases the frequency and duration of episodes of SNA_**

1021 **_in E12.5 embryonic spinal cord._**

1022 A1) Application of 5 µM riluzole inhibits spontaneous giant inward current (GIC) activity in

1023 MNs (voltage clamp recordings; Vh = -60 mV; ECl = -30 mV). A2) Enlarged trace from (A1)

1024 showing GIC before (1, black) and at the onset of riluzole application (2, red). Note that the

1025 amplitude and the duration of GICs were decreased on riluzole application. B1: Box plots

1026 showing the amplitude of the GIC in a control and on riluzole application (n=8). B2: Box

1027 plots showing half amplitude durations of the GIC in control and on riluzole application

1028 (n=8). Note that the amplitude (P < 0.05) and the duration (P < 0.01) of GICs were

1029 significantly reduced in the presence of riluzole. C) Spontaneous network activity (SNA)

1030 recorded at the cervical (C) and lumbar (L) levels (see schematic drawing on the left) in

1031 extracellular configuration before (C1) and after 5 µM riluzole (C2). Note that one episode

1032 still occurred 35 minutes after riluzole application. C3-C6) Box plots illustrating inter-burst

1033 interval, burst duration, intra-burst spike frequency and cervical-lumbar delay of episode
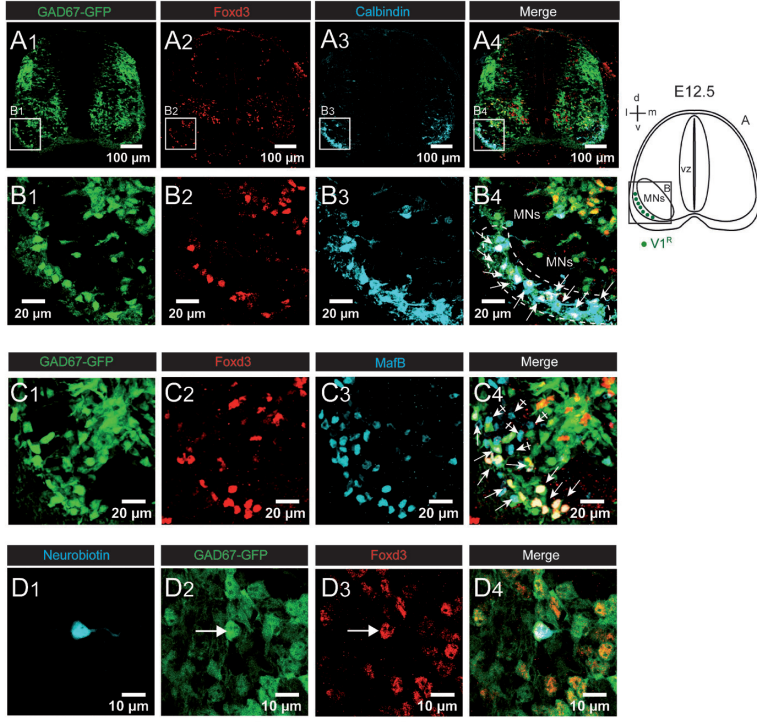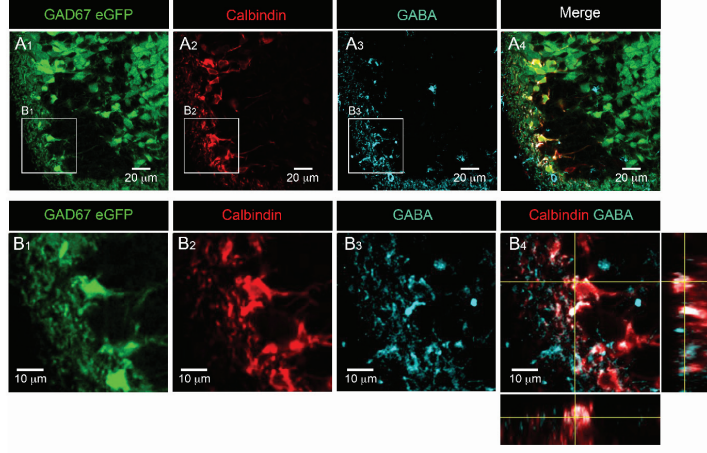
1034 propagation.

1035
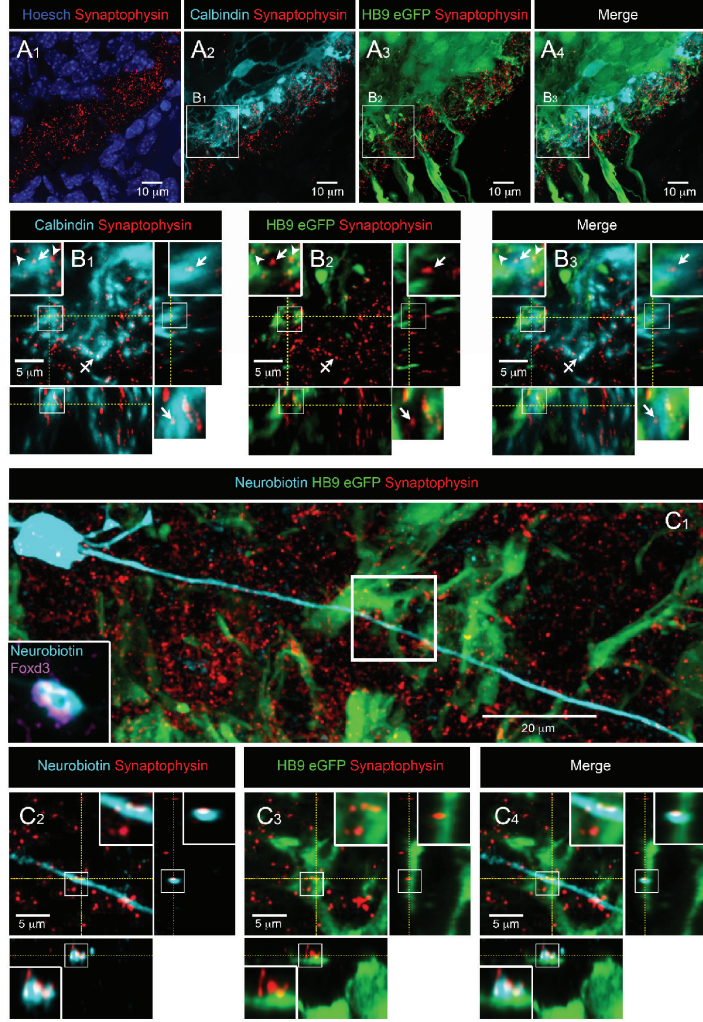
1036 **Table 1 Primary antibodies.**

1037

1038   **Table 2: Intrinsic membrane properties of Renshaw cells**.
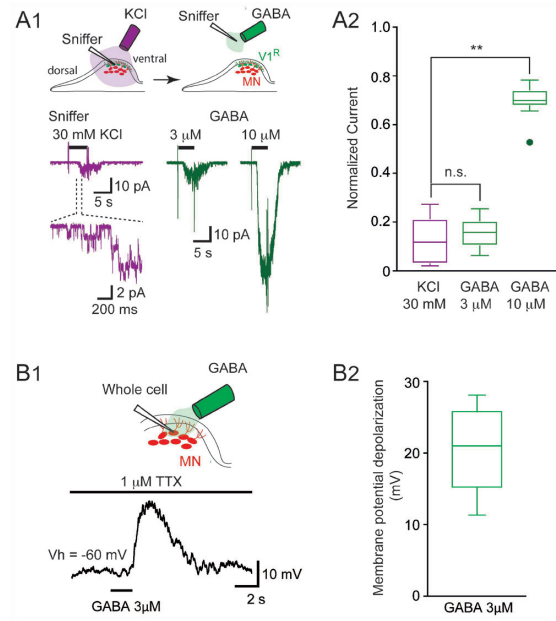
1039   SS-V1^R: single-spiking Renshaw cells, RS-V1^R: repetitive-spiking Renshaw cells, PP-V1^R:

1040   plateau potential Renshaw cells. AP: action potential. Threshold values represent the averaged

1041   action potential threshold for single spiking V1^R and repetitive spiking V1^R and the averaged

1042   plateau potential threshold for plateau potential V1^R. Peak amplitude values represent the

1043   averaged peak amplitude of the action potential for single spiking V1^R, the averaged peak

1044   amplitude of the first action potential in a train for repetitive spiking V1^R and the averaged

1045   peak amplitude of plateau potentials for plateau potential V1^R. Half width values represent the

1046   averaged half width of the action potential for single spiking V1^R, the averaged half width of

1047   the first action potential in a train for repetitive spiking V1^R and the averaged half width of

1048   plateau potentials for plateau potential V1^R. Rate of rise values represent the averaged rate of

1049   rise of the action potential for single spiking V1^R, the averaged rate of rise of the first action

1050   potential in a train for repetitive spiking V1^R and the averaged rate of rise of plateau potentials

1051   for plateau potential V1^R. Values are expressed as mean $\pm$ SD. Input resistance of SS-V1^R,

1052   input resistance of RS-V1^R and input resistance of PP-V1^R were not significantly different (P

1053   = 0.17).

Hoesch Synaptophysin | Calbindin Synaptophysin | HB9 eGFP Synaptophysin | Merge

A₁ | A₂ | A₃ | A₄

Calbindin Synaptophysin | HB9 eGFP Synaptophysin | Merge

B₁ | B₂ | B₃

Neurobiotin HB9 eGFP Synaptophysin

C₁

Neurobiotin Foxd3

Neurobiotin Synaptophysin | HB9 eGFP Synaptophysin | Merge

C₂ | C₃ | C₄

A1 V1^R plateau potential

A2

B1 V1^R repetitive-spiking

B2

C1 V1^R single-spiking

C2

A

0 mV —

0 mV —

20 mV

18 pA   1 s

25pA   5 s

B

0 mV —

0 mV —

20 mV

10 pA   1 s

20 pA   5 s

C

0 mV —

0 mV —

20 mV

30 pA   1 s

20 pA   5 s

D

0 mV —

0 mV —

20 mV

9 pA   1 s

8 pA   5 s

E

- Plateau potential
- Repetitive-spiking
- Mixed
- Single-spiking

21,2 %   28,6 %

8,5 %

41,7 %

F1

0 mV —   control

0 mV —   TTX

20 mV

25 pA

70 pA   1 s

F2

0 mV —   control

0 mV —   TTX

20 mV

1 s

A1

160
80
pA

+20 mV

−100 mV

70 mV/s

TTX

Riluzole

−100 −80 −60 −40 −20 0 20
mV

−20 mV
−100 mV
TTX
Riluzole

100 pA
20 ms

80 pA
60
40
20

mV −60 −40 −20 20

Riluzole

INap TTX sensitive

−20
−40
−60
−80
−100

A2

G_{max} = 0.8 nS
V_{half} = −23.7 mV
k = 8.1

1

0.8

0.6

0.4

0.2

0

Conductance (nS)

−60 −40 −20 0 20
Vh (mV)

B

100

80

60

40

20

0

Max gNap density (pS/pF)

C

Riluzole
(5 µM)

100

80

60

40

20

0

% of control INap

***

A

0 mV —

Control

Riluzole (5 μM)

Riluzole (10 μM)

| 10 mV

50 pA   20 ms

B1

** **

% of control AP amplitude

100
80
60
40
20
0

Ril 5 μM   Ril 10 μM

B2

ns   *

% of control AP threshold potential

100
80
60
40
20
0

Ril 5 μM   Ril 10 μM

B3

*   *

% of control AP half-width

160
140
120
100
80
60
40
20
0

Ril 5 μM   Ril 10 μM

A1 V1^R single-spiking

A2 V1^R repetitive-spiking

A3 V1^R plateau potential

A4 V1^R (E12.5)

A1

Riluzole

1

2

200 pA

2 min

A2

GICs

2

1

200 pA

2 s

B1

Amplitude (pA)

800
600
400
200

*

Cont   Riluzole

B2

Half-width (s)

1.5

1

0.5

0

**

Cont   Riluzole

C1   Control

C

L

C   Episode control

L

20μV

20μV

100 s

20μV

20μV

5 s

C2   Riluzole

C   Episode after 35min riluzole

L

C   Episode after 35min riluzole

L

20μV

20μV

100 s

20μV

20μV

5 s

C3

inter-Burst interval (s)

2000
1500
1000
500

***

Cont   Riluzole

C4

Burst duration (s)

4

3

2

1

0

***

Cont   Riluzole

C5

Max intra burst Frequency (s)

200

150

100

50

0

***

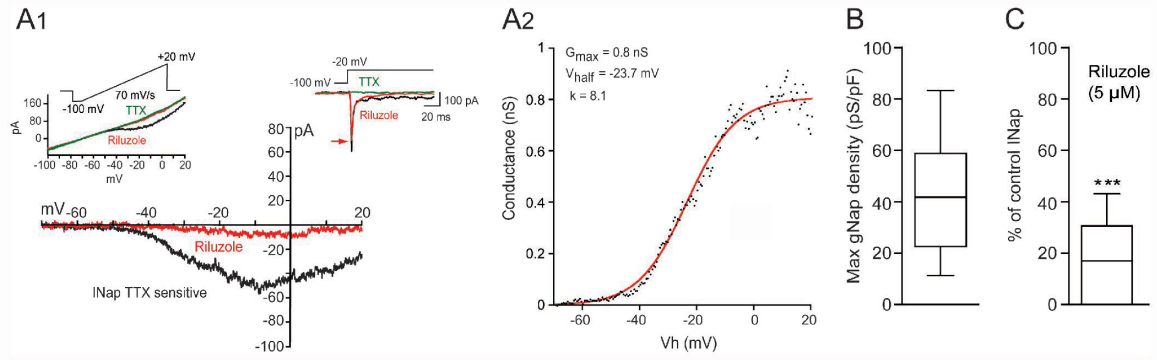Cont   Riluzole

C6

C-L delay (s)

4

3

2

1

0

**

Cont   Riluzole

Table 1. Primary antibodies

Primary antibody	Company	Reference	Host/isotype	Dilution
anti-calbindin-D$_{28k}$	Swant, Switzerland	(Swant Cat# CB38, RRID:AB_2721225)	Rabbit polyclonal	1:1500
anti-FoxD3	provided by C.Birchmeier, MDC Berlin, Germany	Storm R, et al.(2009) Development. ;136:295–305.	Guinea pig polyclonal	1:5000
anti-MafB	Bethyl Laboratories	Bethyl Cat# IHC-00351, RRID:AB_1279487	Rabbit polyclonal	1:1000
anti-GABA	Sigma-Aldrich	Sigma-Aldrich Cat# A0310, RRID:AB_476667	Mouse monoclonal	1:800
Anti-synaptophysin	Synaptic System	Synaptic Systems Cat# 101 011, RRID:AB_887824	Mouse monoclonal	1:1500
Anti-GFP	Aves Labs	Aves Labs Cat# GFP-1020, RRID:AB_10000240)	Chicken polyclonal	1 :1000

	Single-spiking V1^R (SS)	Repetitive-spiking V1^R (RS)	Plateau potential V1^R (PP)
Whole cell capacitance (pF)	13.3 ± 2.8 N = 82	15.3 ± 4.5 N = 60	12.4 ± 3.6 N = 50
Input resistance (MOhm)	1298 ± 682 N = 82	1156 ± 616 N = 60	1254 ± 508 N = 50
Threshold (mV)	-34.1 ± 3.3 N = 46	-33.6 ± 4.9 N = 53	-35.9 ± 6.0 N = 36
peak amplitude (mV)	-6.8 ± 6.1 N = 46	3.2 ± 6.7 N = 53	3.4 ± 10.3 N = 36
half width (ms)	11.2 ± 8.2 N = 46	12.8 ± 6.9 N = 53	705.7 ± 631.7 N = 36
rate of rise (mV/ms)	8.4 ± 3.8 N = 27	13.4 ± 9.4 N = 27	6.2 ± 3.7 N = 19

Table 2: Intrinsic functional properties of V1^R.

SS-V1^R: single-spiking Renshaw cells, RS-V1^R: repetitive-spiking Renshaw cells, PP-V1^R: plateau potential Renshaw cells. AP: action potential. Threshold values represent the averaged action potential threshold for single spiking V1^R and repetitive spiking V1^R and the averaged plateau potential threshold for plateau potential V1^R. Peak amplitude values represent the averaged peak amplitude of the action potential for single spiking V1^R, the averaged peak amplitude of the first action potential in a train for repetitive spiking V1^R and the averaged peak amplitude of plateau potentials for plateau potential V1^R. Half width values represent the averaged half width of the action potential for single spiking V1^R, the averaged half width of the first action potential in a train for repetitive spiking V1^R and the averaged half width of plateau potentials for plateau potential V1^R. Rate of rise values represent the averaged rate of

rise of the action potential for single spiking $V1^R$, the averaged rate of rise of the first action potential in a train for repetitive spiking $V1^R$ and the averaged rate of rise of plateau potentials for plateau potential $V1^R$. Values are expressed as mean ± SD. Input resistance of SS-$V1^R$, input resistance of RS-$V1^R$ and input resistance of PP-$V1^R$ were not significantly different (P = 0.17).